CHANDRA
X-ray Center 60 Garden St., Cambridge Massachusetts 02138 USA

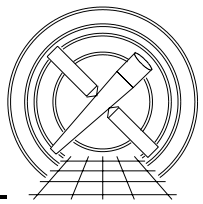

MEMORANDUM

Date: November 3, 2010 15:14
From: T. J. Gaetz
To: File
Subject: Analysis of the *Chandra* On-Orbit PSF Wings
File: `wing_analysis.tex`
Version: `1.0 (Revision B: revised 2010 Nov 03)`

Abstract

This memo presents an analysis of the wings of the *Chandra* point spread function (PSF). The PSF wings result from X-ray scattering from microroughness on the surfaces of the optics. The wings are very faint compared to the direct specular image. In order to study the wings, a deep observation of a very bright high latitude X-ray source (Her X-1, ObsID 3662) is analyzed. Radial profiles are extracted in two ways: In one analysis, the mirror effective area at the position of the specular image is used; this is appropriate for investigating the intrinsic HRMA PSF. The second analysis uses a more conventional exposure map. Radial profiles are extracted, and normalized by a spectrum extracted from the ACIS transfer streak. The profiles are fit to exponentially truncated power laws (with a spatially constant term to model detector background), and the resulting fit coefficients are tabulated.

Pileup metrics are examined, and to be conservative, the fits are restricted to $\theta \gtrsim 15''$. The pileup in the ACIS transfer streak is estimated to be 4%.

Because the mirror scattering is in part diffractive, the diffuse mirror scattering halo is energy dependent; high energy photons tend to be scattered to larger angles than low energy photons. This spectral hardening is also examined.

Contents

List of Tables

List of Figures

1 Introduction

The PSF of the *Chandra* High Resolution Mirror Assembly (HRMA) includes contributions ranging from nearly specular reflection from low frequency figure errors (the "core" of the PSF) to scattered photons reflecting/diffracting off of surface microroughness on the optics (the "wings" of the PSF). The scattered photons form a faint diffuse halo extending to large angles. The *Chandra* on-axis PSF can thus be approximately divided into two limiting regimes (see Fig. 1):

- *core*, consisting of quasi-specular X-rays reflecting from the mirror surface (including the effects of low-frequency mirror figure errors, deformations, and misalignments)
- *wings*, consisting of reflected/diffracted X-rays which scatter off the high spatial frequency components of the surface. The wings are energy dependent. The on-axis azimuthally-averaged wing profile falls approximately as $\theta^{-\gamma}$, where θ is the angular distance from the core and $\gamma \sim 2$.

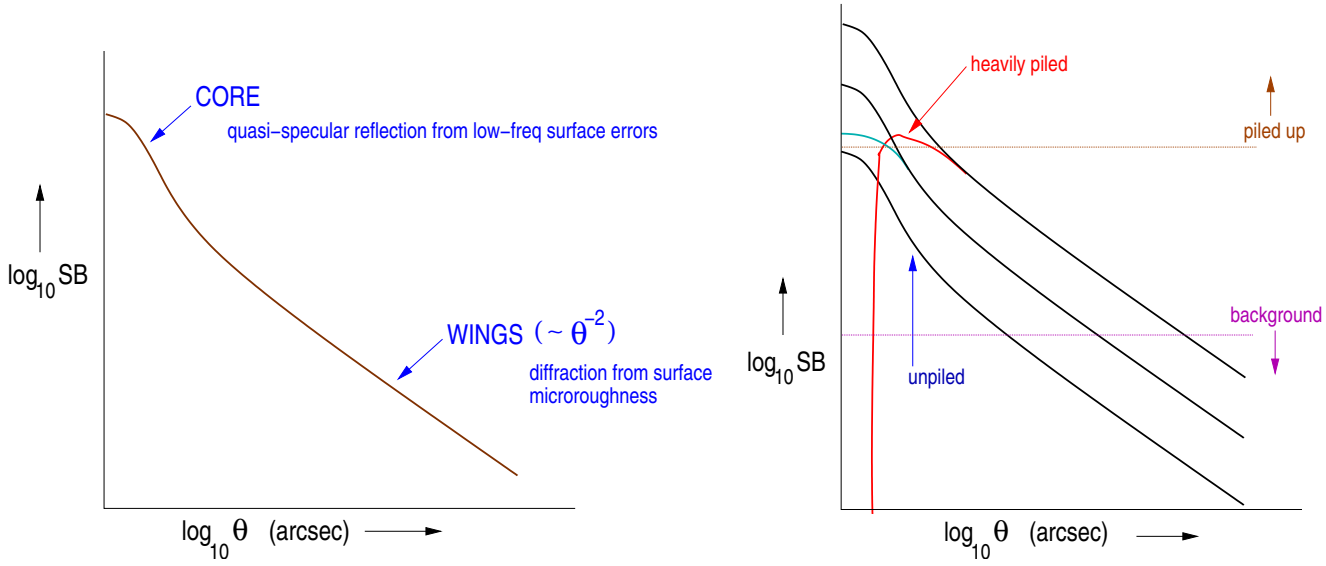

Figure 1: Left: Schematic of the on-axis PSF as a function of angular distance from the core. Right: Schematic of the effects of detector pileup and background. Count rate per pixel above some limit results in pileup. The pileup modifies the event grades ("grade migration"), which for serious enough degradation, results in loss of the event. Detector and sky background limits how low the source count rate per pixel can be detected.

In order to better understand the PSF and the wings as a function of energy, on-orbit data using ACIS as the detector is needed. Because of detector pileup, ACIS has a relatively limited dynamical range. The detector evaluates event positions and energies based on the charge detected within 3×3 pixel islands. If more than one event contributes

significant charge to an island within the frame accumulation time (typically 3.2 seconds), the energy of the detected event is perturbed; with severe pileup, the event is no longer detected as a valid X-ray event. This presents formidable problems for studying the PSF. The core of the *Chandra* PSF is very narrow (subpixel) and its study requires very faint sources in order to avoid pileup. The far wings are very faint compared to the core: a very bright source is needed in order to see the wings with good statistics above the detector background, but this results in heavy pileup in the core and inner wings, complicating the assessment of the intrinsic source rate. When using astronomical sources, great care is also needed to avoid building astrophysics into the calibration. For example, any intervening dust column will scatter X-rays and produce an X-ray dust scattering halo. Cosmic dust scattering is most important at low energies; the total dust-scattered power scales roughly as E^{-2}, but at fixed angle, the amplitude scales very roughly as E^{-1}. In order to minimize the effects of dust halos, it is necessary to use sources with as low an N_H column as possible. Another potential contaminant is diffuse emission such as emission from the galaxy hosting an active galactic nucleus (AGN). Consequently, the most promising candidates are stellar sources and compact objects at high galactic latitude.

In this memo, an analysis of the *Chandra* wings based on a deep observation of Her X-1 (ObsID 3662) is presented. Some aspects are preliminary. In particular, the ACIS optical blocking filters have a nonuniform contamination layer which reduces the effective quantum efficiency (QE) of the detector in a spatially and energy dependent manner. The effect of this contamination is most significant for low energies, and negligible at high energies. Because of this, there remain uncertainties in the PSF wing profiles and normalization below ~ 1 keV. Investigations of the azimuthal dependence of the wings have also been postponed.

The organization of this memo is as follows. In §2, the Her X-1 observation (ObsID 3662) is described. The data reduction, extraction of radial profiles, and treatment of the effective area and exposure correction are discussed in §3. In §4 the analysis of the profiles is discussed. The core and inner wings for this observation are heavily piled up, so to be conservative, the profile fits are performed only for radii $\gtrsim 15''$; pileup estimation for the wings and for the transfer streak is discussed in Appendix A. The profiles are fitted using powerlaws with an exponential cutoffs, and plots and fit parameters for the wings in broad energy bins ($\Delta E = 1$ keV) are provided. These fits are to profiles constructed without including mirror vignetting in the exposure correction; see Appendix C for a discussion. The corresponding fits with the mirror vignetting included are provided in Appendix D. The profiles are normalized using the spectrum extracted from the ACIS transfer streak from the core and scaling for the frame transfer duty cycle; the normalization calculations are discussed further in Appendix B.1 and Appendix B.2. In §5, the main features of the analyses are summarized, and caveats on the interpretation are discussed.

Because the mirror scattering is in part diffractive, the scattering angle depends on energy - for a given roughness and angle of incidence, high energy photons will scatter to larger angles than low energy photons. Consequently, the diffuse mirror scattering wings tend to harden with increasing angle from the core; this is discussed in Appendix E where spectra extracted from concentric annular regions are presented. Finally, Appendix F discusses the anomalous line feature near 1.5 keV in the diffuse spectrum at large radii; its origin is unknown, but it is believed to be a telescope artifact, possibly resulting from

the extremely bright source and the configuration used.

2 The Observation

In order to calibrate the far wings of the PSF, Her X-1 was observed. Her X-1 was selected because it is a very bright source (in its high state) at high galactic latitude ($b = 37.52$), with low extinction ($E[B-V] < 0.05$; see Liu et al. (2000)). The total galactic column in that direction is $N_{\rm H} \sim 1.8 \times 10^{20}\,{\rm cm}^{-2}$ (Dickey & Lockman, 1990). The total X-ray cosmic dust scattering halo is likely $\lesssim 1.5\%$ (Smith et al., 2002). Her X-1 was observed by *Chandra* for 50 ks on July 1-2, 2002, imaged on a corner of the ACIS S3 chip with the detector translated to place the image $\sim 45''$ from the optical axis (see Fig. 2). Although the source is somewhat off-axis, this does not significantly affect the far wings — $0.75'$ is much smaller than the mean graze angle of the smallest mirror pair ($\sim 27'$). The ACIS I2, I3, and S2 chips were also on to provide additional coverage. The nominal ACIS frame time was 3.1 seconds. The Very Faint (VF) Timed Exposure (TE) mode was used, although the current study does not apply VF filtering. The radiation environment was quiescent (no flares) and the background, evaluated for 11–13 keV, was 4.83% higher than that for the appropriate blank sky background dataset (acis7sD20001201bkgrndN002.fits).

Table 1: Summary of the Observation

	ObsID	Object	Exposure	Frame Time	θ	$N_H(\ {\rm cm}^{-2})$
Wings	3662	Her X-1 high state	50 ks	3.1 s	$45''$	1.8×10^{20}

In Fig. 3, part of the derolled image of the Her X-1 ObsID 3662 observation is plotted, with the ACIS transfer streak and the strut shadows indicated. The strut shadows are caused by the mirror support struts. The presence of these shadows indicates that the diffuse halo is predominantly caused by in-plane mirror scattering rather than a diffuse astrophysical halo due to dust scattering along the line of sight. The image of a diffuse astrophysical halo would be the superposition of many images like Fig. 3 which would tend to fill in the shadows. A portion of the azimuthal profile (1–2 keV, $1'$–$2'$ from the source, 1° bins in azimuth ϕ) is shown in right panel of Fig. 3. The depth of the shadows indicate that any cosmic dust halo contribution cannot be more than $\sim 1/4$ of the observed halo, confirming that the diffuse halo is primarily caused by mirror scattering.

3 Data Reduction

The data were reprocessed without pixel randomization, starting with the level 1 event lists. In this initial analysis, I consider ACIS-S3 data only. Very Faint filtering is not applied at this time.

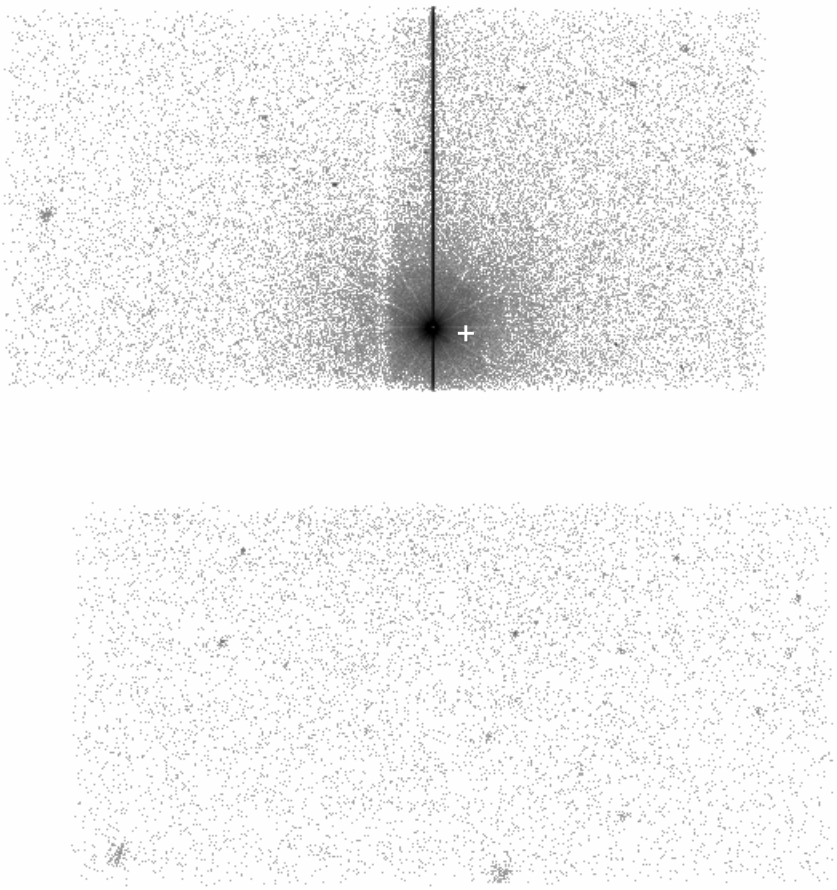

Figure 2: Derolled image of the Her X-1 wings observation, ObsID 3662. The event list was energy filtered (0.5-2.0 keV) to reduce the background. The white '+' indicates the location of the nominal optical axis during the observation.

Ultimately, extracting the PSF is a combined spatial/spectral problem: one wants the spatial profile of the wings as a function of energy. Unfortunately, there do not currently exist tools to deal easily with a combined spatial/spectral analysis. The approach I have taken is to construct narrow-band count images. The bands are $\Delta E = 0.1$ keV for 0.4–2.2 keV, $\Delta E = 0.2$ keV for 2.2–8.0 keV, and $\Delta E = 0.5$ keV for 8.0–10.0 keV. For the same energy bins, dithered QE maps are constructed using the *CIAO*[1] tools `mkinstmap` to construct the QE map and `mkexpmap` to project the QE map to the sky, including the effects of dither. In using `mkinstmap`, the HRMA effective area is excluded, resulting in effective QE maps rather than conventional exposure maps (see Appendix C for a

[1] *CIAO* is a set of analysis tools produced by the *Chandra* X-ray Center. See `http://cxc.harvard.edu/ciao/`.

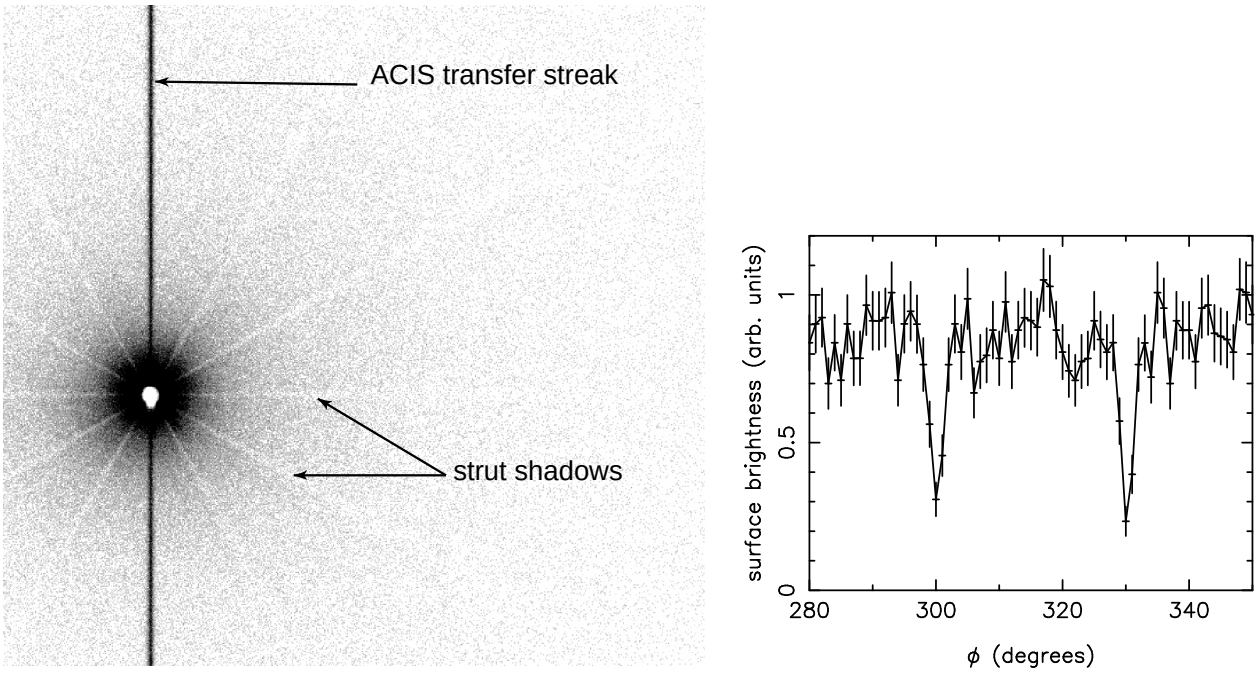

Figure 3: Left: Closeup of the deep Her X-1 wings observation. The ACIS transfer streak results from photons hitting the detector during the frame transfer to the frame store. The observation is notable for showing the shadows produced by the mirror support struts. Right: azimuthal variation of the 0.5–2.0 keV diffuse emission 1–2′ from the source; 1° bins in ϕ.

discussion; the alternative approach of including the mirror vignetting in the exposure map calculation is presented in Appendix D). The mirror effective area is evaluated separately for a small (10″ radius) region centered on the position of the specularly imaged source. Exposure-corrected images are then formed by dividing the counts images by the dithered QE maps, the total exposure time, the effective area at the source position, and a correction for the low-energy QE degradation (see Eq. 1). These corrected images are combined into broader (1 keV wide) band images; the sum is weighted to account for an approximate treatment of the energy-dependence of the low energy QE degradation from the ACIS contaminant.

For ObsID 3662, the effect of background is evaluated using the appropriate blank sky background data (acis7sD20001201bkgrndN002.fits) obtained from the *Chandra* calibration database[2]. The sky background dataset is reprojected to the sky using the *CIAO* tool `reproject_events` with the ObsID 3662 aspect solution. Narrow-band counts and dithered QE maps are constructed, and exposure-corrected images are constructed in the same way as for the wings data. As noted in §2 the radiation environment was quiescent; based on comparing the rates for 11–13 keV, the background dataset is rescaled by 1.0483.

[2]http://cxc.harvard.edu/caldb/

3.1 Radial Profiles

Note that the treatment in this section is aimed at extracting the intrinsic PSF shape. As noted in Appendix C, X-rays scattered by the optics will be vignetted differently than imaged X-rays from celestial sources; Appendix D provides a treatment more appropriate for comparing to sky sources.

Radial profiles are extracted using annular regions centered on the source. The radial binning is variable: the inner bins are defined as $\theta_i = \theta_{i-1} + \Delta\theta$ where $\Delta\theta = 2''$, but beyond $20''$, the radii increase faster than linearly as $\theta_i = 1.1 \times \theta_{i-1}$. Asymptotically, this provides approximately logarithmic binning. For logarithmic binning, a powerlaw $\propto \theta^{-2}$ would produce approximately the same number of source counts in each bin (although the included background counts would be increasing with radius). Extraneous sources are excised from the annular regions, and the regions are also clipped near chip boundaries (allowing for the extent of the dither pattern). The ACIS transfer streak for the bright central source significantly contaminates the profile at large θ. A narrow (10 pixel wide) rectangle centered on the streak is therefore excised.

For each energy band, radial surface brightness profiles are constructed from the counts image and from the QE and exposure corrected images; the counts image data are used to propagate errors for the QE and exposure-corrected data. This results in surface brightness profiles for the quantity

$$\langle \psi_{src} \rangle_{\Delta\theta_i} = \frac{\langle C_{src,corr} \rangle_{\Delta\theta_i}}{A_{\mathit{eff},src}\, t_{src,exp}} \quad (\mathrm{ct\,s^{-1}\,arcsec^{-2}}) \tag{1}$$

where $C_{src,corr} = C_{src,counts}/q\,\mathcal{Q}$ is the QE-corrected counts image, A_{eff} is the effective area at the source position (see Appendix C), t_{exp} is the exposure time, and q is a (spatially independent) correction factor for the low-energy QE degradation at the time of the observation ($\simeq 1$ for $E \gtrsim 1$). The $\langle\rangle_{\Delta\theta_i}$ indicates an average over annulus i of width $\Delta\theta_i$ and also over the energy band ΔE.

The surface brightness for background is constructed in the same way using the sky background dataset:

$$\langle \psi_{bgd} \rangle_{\Delta\theta_i} = \frac{\langle C_{bgd,corr} \rangle_{\Delta\theta_i}}{A_{\mathit{eff},src}\, t_{bgd,exp}} \quad (\mathrm{ct\,s^{-1}\,arcsec^{-2}}) \tag{2}$$

For consistency with the source profile calculation, the effective area at the source, A_{eff} is used. The correction factor, q, for the low energy QE degradation is not applied for the background (predominantly charged particle events).

3.2 Normalizing the profiles

The treatment outlined in §3.1 still includes the underlying spectrum of the source. The surface brightness therefore needs to be normalized. Ideally one would use the integral over the PSF profile out to some fiducial distance. In the case of the deep wings observation, almost all of the directly imaged photons are lost to extreme pileup in the core with grade migration into bad events, so an alternative approach must be found. An attempt was made to match the profile to a zero-order HETG grating image of the

source in a low state. Unfortunately, the profile obtained for this ACIS/HETG observation disagrees significantly with a deep HRC-I observation of AR Lac (Gaetz *et al.* 2003 *Chandra* Calibration Workshop Presentation)[3]. A stack of observations of faint sources (mostly HETG grating zero order images) also shows this effect (Jerius *et al.* 2003 *Chandra* Calibration Workshop Presentation)[4] Currently, the normalization derived from the ACIS transfer streak is believed to be more reliable than matching profiles, although some properties of the transfer streak properties remain uncertain. In the following, a normalization based on the transfer streak spectrum is used. The normalization calculation is discussed further in Appendix B.

4 ANALYSIS

4.1 Pileup

Because of the extreme brightness of the source, the central regions of the profile are heavily piled up, and we need to know how far out the profile is affected by pileup. Several approaches for assessing pileup are discussed in Appendix A; based on these pileup diagnostics, I estimate that pileup is significant inside a radius of $\sim 8''$, and possibly as far as $\sim 15''$. Although radial profiles may be extracted for radii $< 15''$, to be conservative, only data for $\geq 15''$ are included in the fits.

4.2 Preliminary Powerlaw Fits

The first stage of the analysis is to fit powerlaw profiles to the radial profiles extracted for the narrow-band Her X-1 wings data:

$$\psi(\theta) = a \left[\frac{\theta}{\theta_0} \right]^{-\alpha} + b \tag{3}$$

where b is the background component, a is the wing amplitude scale factor, α is the powerlaw slope, and $\theta_0 \equiv 10''$ is a reference radius. These are simultaneous fits to a powerlaw plus constant background to both the Her X-1 dataset and the corresponding blank sky background dataset; the powerlaw amplitude is frozen at 0 in the background dataset fits.

The powerlaw slopes are plotted as a function of energy in Fig. 4. The profiles are steep at low energies, rapidly becoming shallower toward ~ 1.8 keV. Below ~ 1 keV, the low-energy QE degradation is very important; an approximate correction has been applied, but the magnitude and spatial nonuniformity of the effect are still under investigation. Consequently, the derived powerlaw indices for $E \lesssim 1$ keV are somewhat uncertain. The powerlaw slope is fairly constant for ~ 1.8–5.0 keV, and steepens again above ~ 5 keV. The steepening above 5 keV is likely the result of the roughest mirror pair (MP1) dropping out as its effective area rapidly declines with increasing energy.

[3]http://cxc.harvard.edu/ccw/proceedings/index.html/presentations/gaetz/index.html
[4]http://cxc.harvard.edu/ccw/proceedings/index.html/presentations/jerius/index.html

Because of pileup effects, the wings are fit only for $\theta \geq 15''$. The radial profiles for the Her X-1 dataset are fit simultaneously with profiles extracted from the sky background dataset; the background contribution is fit as a constant.

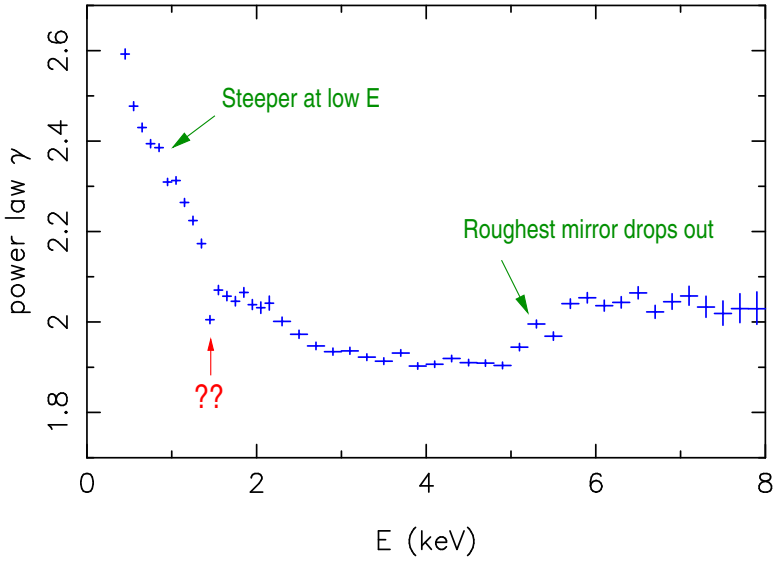

Figure 4: Powerlaw index for fits to the narrow band ObsID 3662 data. See text and Appendix F for further discussion of the "glitch" near 1.5 keV.

In examining the powerlaw slopes more carefully, a glitch in the trend was noted at 1.5 keV. Further investigation uncovered an anomalous line feature in the diffuse emission at 1.5 keV which does not appear in the background spectrum or in a spectrum extracted from the transfer streak. This feature is believed to be a telescope artifact, although its origin is not currently understood. This analysis is discussed further in Appendix F. The 1.4–1.6 keV region was removed from the analysis and the band filled by interpolating from the adjacent energy bands.

4.3 Powerlaw plus Exponential Cutoff Fits

To improve the statistics in the profiles, the very narrow band data were combined into 1 keV bands and fit in the same way as in §subsec:fitting.the.profiles. These profile tend to be shallower than the best fit powerlaw at smaller angles, and steeper at large angles. In order to allow for this behavior, the wing profile is fit by a powerlaw plus exponential cutoff plus spatially constant background:

$$\psi(\theta) = a \left[\frac{\theta}{\theta_0}\right]^{-\alpha} \exp\left(c\theta\right) + b \tag{4}$$

where b is the background component, a is the wing amplitude scale factor, α is the powerlaw slope, and $1/c$ is the exponential cutoff scale length. The fit is scaled to a

reference radius, $\theta_0 \equiv 10''$. The background datasets are fit with the a parameter frozen at 0. The resulting fits are plotted in Figs. 5-8.

For comparison, models based on the ground calibration data are overplotted.[5] Above $\sim$ 2 keV and beyond $\sim 15 - 20''$, the profiles are reasonably consistent with the model constructed based on ground calibration data. The on-orbit wings tend to have a slightly shallower slope, consistent with expectations: in the ground experiments, the nonuniform illumination undersampled the rougher ends of the optics, and the rougher regions would be expected to scatter more. The profiles for the ground data show an upward curvature toward smaller θ which is not seen in the on-orbit profiles. Although pileup becomes significant as the core of the PSF is approached, it does not seem sufficient to explain the differences $\sim 10 - 20''$ from the core. Ground measurements of the wings were not obtained for the HRMA as a whole. Instead, the model is based on combining data for individual quadrants of individual mirror pairs at a sparse set of energies into "Power Spectral Densities" (PSDs; functions of spatial frequency of the surface microroughness). The four individual PSDs (one for each mirror pair) are combined into a surface brightness profile, taking into account the photon energy, the mean graze angle for each mirror pair, and weighted by the fractional effective area. The steepening in the model originates in the models for the inner two mirror pairs; it may be an artifact of the fitting process and systematics in the data and of various stages of the analysis. Based on current understanding, it is believed that the true wings for $E \lesssim 20''$ are intermediate between the on-orbit estimate and the ground-based estimate, but likely closer to the on-orbit value. However, pileup (increasingly important in this dataset inside $\sim 10 - 15''$ would have the effect of reducing the slope toward smaller radii.

[5] See memo: http://cxc.harvard.edu/cal/Hrma/psf/XRCF_PSF_wing_profile/

Table 2: Fit Parameters. (Note: errors are purely statistical.)

Energy (keV)	γ	a (ct arcsec^{-2})	c (arcsec^{-1})	b (ct arcsec^{-2})	χ^2(dof)
1.0-2.0	1.972 ± 0.003	$(0.748 \pm 0.004) \times 10^{-05}$	$(-0.675 \pm 0.049) \times 10^{-03}$	$(0.373 \pm 0.003) \times 10^{-08}$	246(70)
2.0-3.0	1.840 ± 0.004	$(1.012 \pm 0.007) \times 10^{-05}$	$(-1.212 \pm 0.060) \times 10^{-03}$	$(0.525 \pm 0.004) \times 10^{-08}$	70(70)
3.0-4.0	1.760 ± 0.008	$(1.875 \pm 0.016) \times 10^{-05}$	$(-1.963 \pm 0.052) \times 10^{-03}$	$(0.661 \pm 0.007) \times 10^{-08}$	104(70)
4.0-5.0	1.749 ± 0.008	$(2.569 \pm 0.022) \times 10^{-05}$	$(-1.982 \pm 0.051) \times 10^{-03}$	$(0.840 \pm 0.009) \times 10^{-08}$	75(70)
5.0-6.0	1.902 ± 0.011	$(3.471 \pm 0.037) \times 10^{-05}$	$(-1.783 \pm 0.074) \times 10^{-03}$	$(1.406 \pm 0.015) \times 10^{-08}$	133(70)
6.0-7.0	1.948 ± 0.015	$(4.017 \pm 0.059) \times 10^{-05}$	$(-1.844 \pm 0.116) \times 10^{-03}$	$(3.177 \pm 0.030) \times 10^{-08}$	98(70)
7.0-8.0	2.137 ± 0.030	$(4.909 \pm 0.128) \times 10^{-05}$	$(0.333 \pm 0.253) \times 10^{-03}$	$(16.605 \pm 0.116) \times 10^{-08}$	121(70)

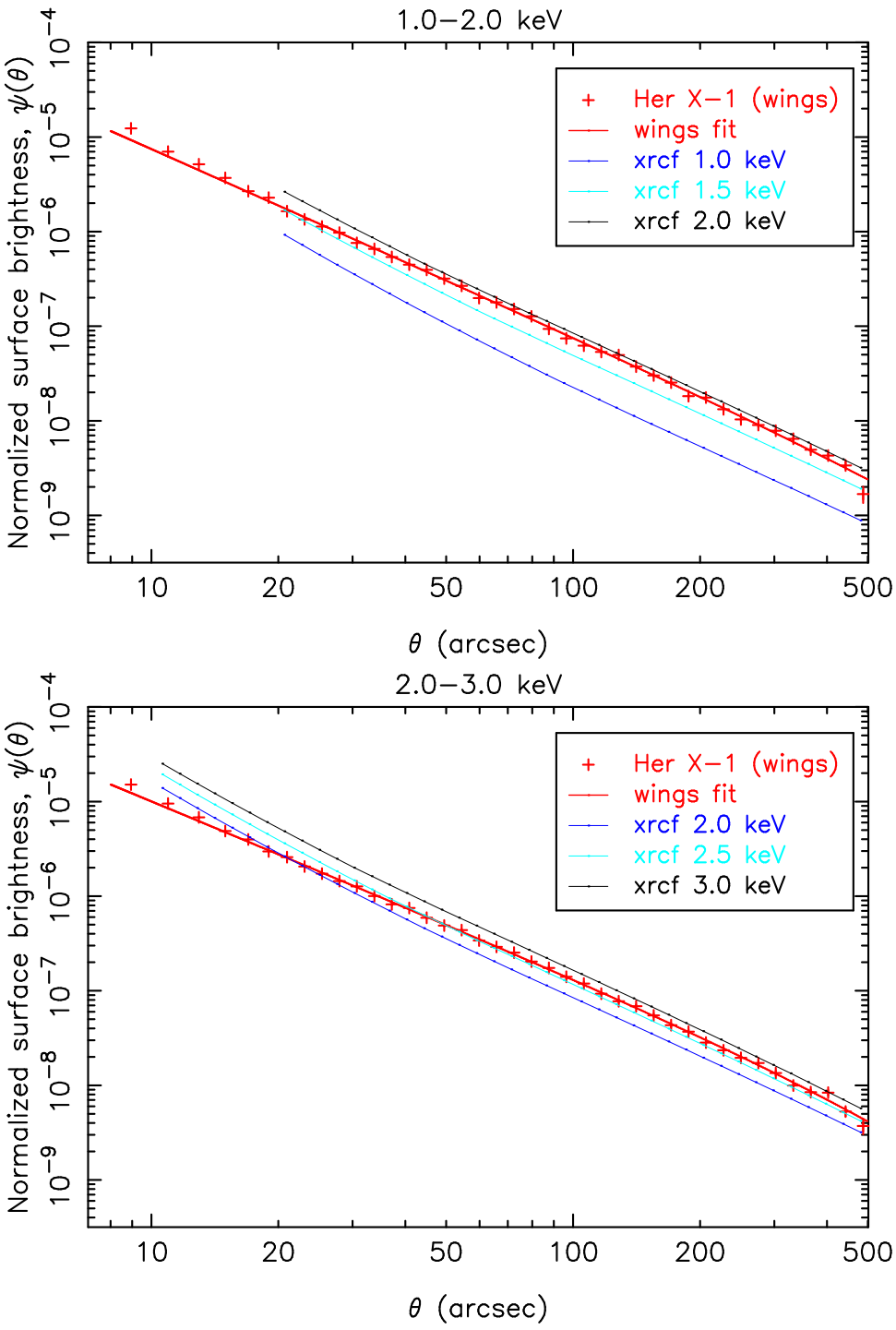

Figure 5: Powerlaw plus exponential cutoff fits to the obsid 3662 (Her X-1 wings) data; the fits were for $\theta \geq 15''$. The model based on ground calibration data is also indicated (labeled "xrcf"). Top: 1.0-2.0 keV. Bottom: 2.0-3.0 keV.

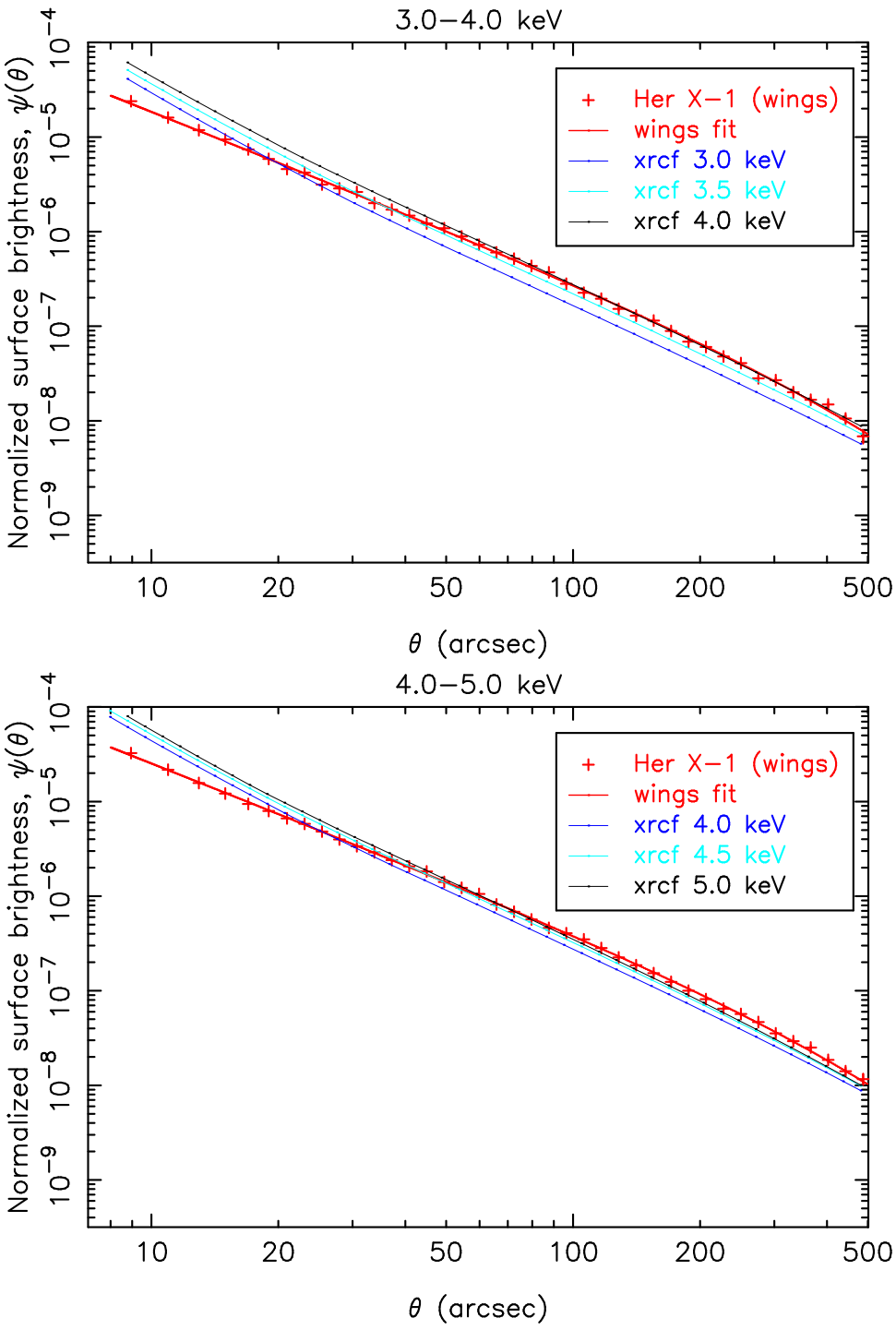

Figure 6: Powerlaw plus exponential cutoff fits to the obsid 3662 (Her X-1 wings) data; the fits were for $\theta \geq 15''$. The model based on ground calibration data is also indicated (labeled "xrcf"). Top: 3.0-4.0 keV. Bottom: 4.0-5.0 keV.

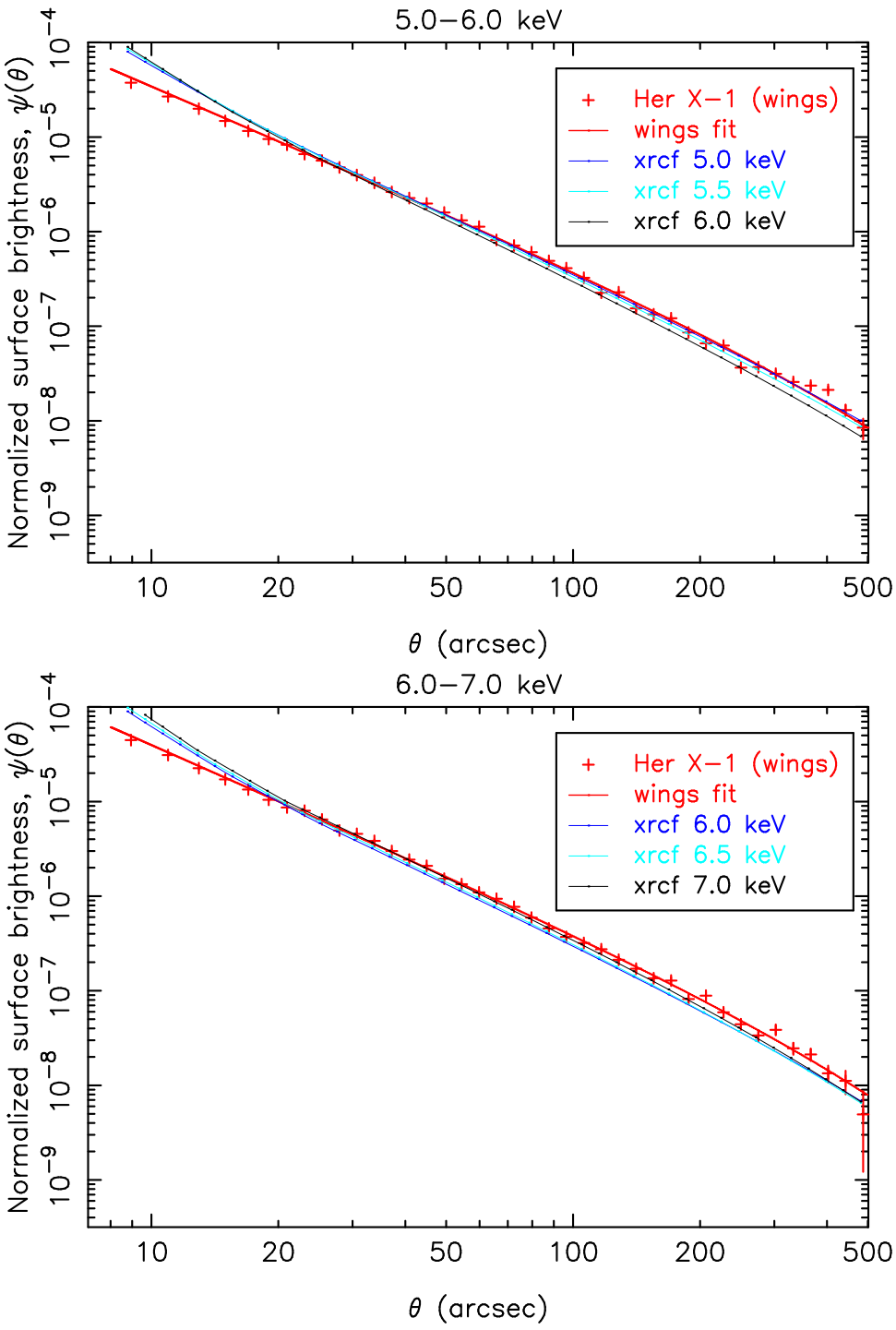

Figure 7: Powerlaw plus exponential cutoff fits to the obsid 3662 (Her X-1 wings) data; the fits were for $\theta \geq 15''$. The model based on ground calibration data is also indicated (labeled "xrcf"). Top: 5.0-6.0 keV. Bottom: 6.0-7.0 keV.

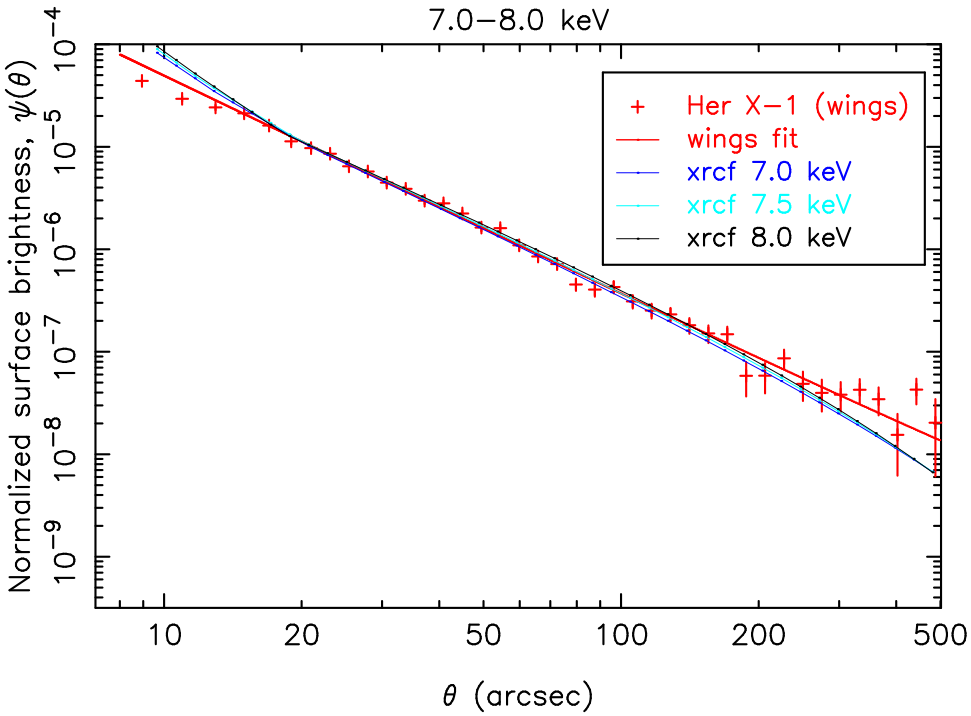

Figure 8: Powerlaw plus exponential cutoff fits to the obsid 3662 (Her X-1 wings) data; the fits were for $\theta \geq 15''$. The model based on ground calibration data is also indicated (labeled "xrcf"). 7.0-8.0 keV.

Because of the form of the fit, the local powerlaw slope varies as a function of energy and θ, illustrated in Fig. 9. The asymptotic slope is steepening with energy; the highest energy bin (7–8 keV) has poor statistics at large radii, and the shape of the profile is relatively poorly constrained. For the energy bins below 7 keV, the curvature of the profile increases up to $\sim$ 4–5 keV, then stays relatively constant, but with the overall slope very gradually steepening.

5 Summary and Caveats

The deep observation of Her X-1 (ObsID 3662) provides the most detailed information available on the on-orbit (nearly) on-axis wings of the *Chandra* PSF. In the present study, the wings are examined for relatively broad energy bands ($\Delta E = 1$ keV) so that the wings can be followed with good statistics to large distances from the specular image. For $E \leq 7$ keV, the profiles can be followed out to $\sim 8'$; beyond $8'$, the statistics for the S3 profiles deteriorate rapidly as the surface brightness falls and a larger fraction of each annulus falls off the detector. As can be seen in Fig. 8, the profile can be followed out to at least $5'$ even for for the 7–8 keV band (although the poor statistics for the 7–8 keV do not provide very good constraints on the profile shape). The additional data on S2, I2, and I3 may allow the profile to be probed further out.

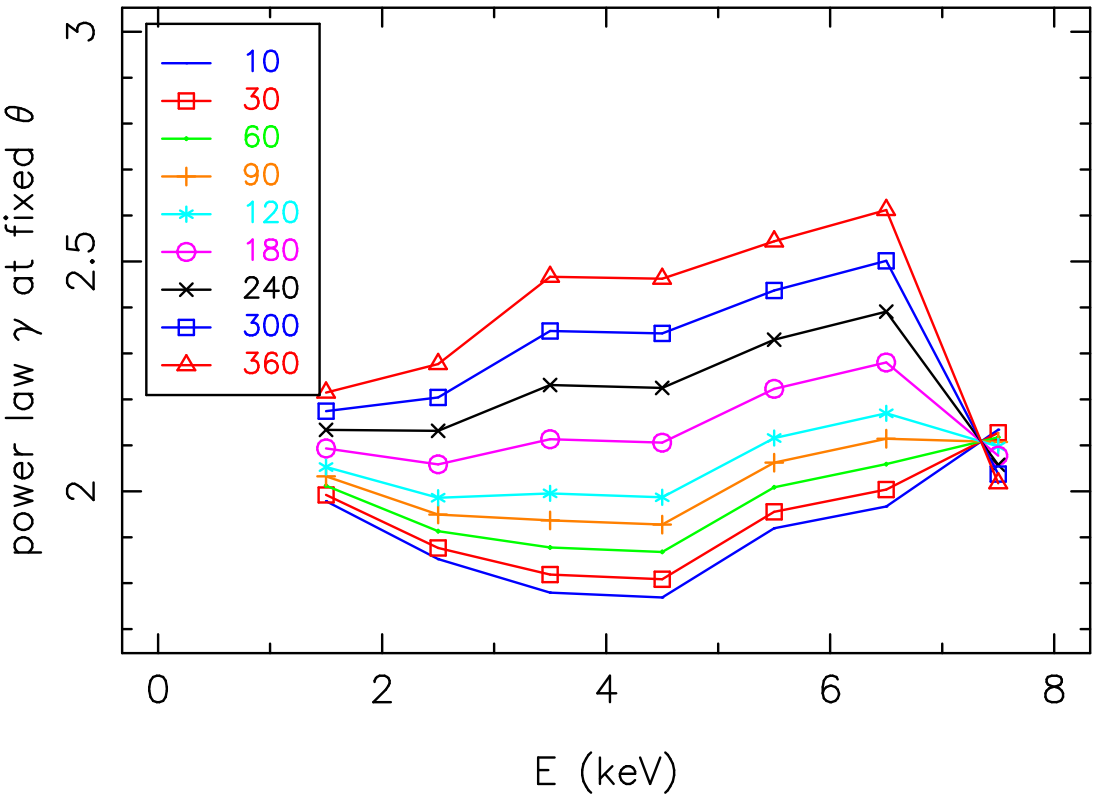

Figure 9: Variation in local powerlaw slope. The curves are labeled by the value of θ in arcsec. The highest energy band (7–8 keV) is poorly constrained; the flatter profile is likely influenced by uncertainties in the background subtraction.

The data are analyzed by constructing narrow band counts images and normalizing them using a dithered QE map and the mirror effective area and vignetting at the position of the specular image of Her X-1. (An alternative treatment using a more conventional exposure map which includes mirror vignetting at the detected event position is included as Appendix D; see Appendix C for further discussion.) An approximate treatment of the low energy QE degradation resulting from the ACIS contamination is included, but this includes only the spectral distribution and does not contain the spatially dependent component; the effect of the spatially-dependent contamination component is negligible at high energies, but is an important effect below $\sim$ 1 keV, and becomes increasingly important as energy decreases.

The extracted radial profiles are fit by a powerlaw with an exponential cutoff and a spatially constant background term (Eq. 4). Profiles for the Her X-1 observation, and corresponding profiles for a blank-sky dataset are fit simultaneously; the profiles for the blank sky data are rescaled upward by 4.8%, based on comparing the Her X-1 ObsID 3662 data and the blank sky data for 11–13 keV.

The fits are for 1 keV wide bands from 1-2 keV to 7-8 keV. Below 1 keV the results

are very uncertain because of the energy and spatial dependence of the absorption from the contamination layer on the ACIS optical blocking filter. Above 7–8 keV, the statistics rapidly become poorer. The fits parameters are listed in Table 2 and the fits are plotted against the data in Figs. 5-8; for reference, model based on ground measurements[6] are also plotted. (The corresponding parameters and plots for profiles derived using a more conventional exposure map given in Table D.1 and Figs. D.1-D.4.)

Above ~ 2 keV and beyond $\sim 15-20''$, the profiles are reasonably consistent with the model constructed based on ground calibration data. The on-orbit wings tend to have a slightly shallower slope, consistent with expectations: in the ground experiments, the nonuniform illumination undersampled the rougher ends of the optics, and the rougher regions would be expected to scatter more. The profiles for the ground data show an upward curvature toward smaller θ which is not seen in the on-orbit profiles. Although pileup becomes significant as the core of the PSF is approached, it does not seem sufficient to explain the differences $\sim 10-20''$ from the core. This is believed to result from artifacts and systematic errors in combining the ground data.

Based on current understanding, it is believed that the true wings for $E \lesssim 20''$ are intermediate between the on-orbit estimate and the ground-based estimate, but likely closer to the on-orbit value. However, pileup (increasingly important in this dataset inside $\sim 10-15''$) would have the effect of reducing the slope toward smaller radii.

The normalization of the profiles is also subject to systematic errors. In order to put the profiles on the same footing so that they can be directly compared (and scaled), the surface brightness should be scaled by the total exposure-corrected count rate of the source over the corresponding energy band. Because of extreme pileup, removes most of the directly imaged photons are lost, a direct estimate of the count rate are not available. In this memo, the profiles have been normalized using a spectrum extracted from the events accumulated during ACIS frame transfer. The frame transfer time is much shorter than the frame accumulation time, so the transfer streak events are much less susceptible to pileup; in this observation, the QE degradation for transfer streak events is estimated to be $\sim 8\%$. In addition, no aperture correction for the pileup extraction region has been applied to account for the PSF wing contribution falling outside the narrow ($10''$-wide) transfer streak extraction region. This is estimated to be at most a 5–10% effect.

[6] http://cxc.harvard.edu/cal/Hrma/psf/XRCF_PSF_wing_profile/

6 References

References

Dickey, J. M. & Lockman, F. J. 1990, ARA&A, 28, 215

Heinke, C. O., Edmonds, P. D., Grindlay, J. E., Lloyd, D. A., Cohn, H. N., & Lugger, P. M. 2003, ApJ, 590, 809

Liu, Q. Z., van Paradijs, J., & van den Heuvel, E. P. J. 2000, A&AS, 147, 25

Smith, R. K., Edgar, R. J., & Shafer, R. A. 2002, ApJ, 581, 562

A Pileup

If two or more events within a single frame occur close enough to each other spatially that the their charge clouds significantly overlap, the event(s) are piled up. The excess charge from the overlapping cloud distorts the event energy (causing the reported event energy to be too high), and modifies the distribution of charge within the 3×3 pixel event "island", thus altering the event grade ("grade migration"). Grade migration tends to spread charge into more pixels, degrading the quality of the event; the frequency of grade 0 (single pixel) events decreases while that for grade 6 events increases. In addition, events with *ASCA* "good" grades (grades 0,2,3,4,6) can be converted into *ASCA* "bad" grades (grades 1,5,7). If the event morphs into a sufficiently bad grade, it may end up in one of the grades outside the *ASCA* grade set; the event may be filtered out onboard in which case it does not appear in the telemetry stream.

Pileup thus affects the data by distorting the spectrum (making the spectrum appear harder) and depressing the effective QE for the piled up events. The event rate is decreased as merged events are reported as a single event. Pileup is mostly a concern for bright point sources close to on-axis. The narrow PSF core results in photons repeatedly landing in single pixels. As the telescope dithers, the aimpoint shifts by only a small fraction ($\lesssim 1/3$) of a pixel during the frame collection time. Pileup can also be a problem for sufficiently bright diffuse emission.

In the Her X-1 (ObsID 3662) observation, the source is bright enough that the far core and near wings are piled up. (The core itself is so heavily piled up that a hole appears in the profile, even in the level 1 event list; most of the core events are filtered out onboard.) The surface brightness for the on-axis PSF falls with increasing distance from the core, so the degree of pileup also falls with distance from the core. The determination of pileup is important for understanding this observation: we need to know how far into the core the profile can be extended before pileup becomes an issue. A number of approaches for assessing pileup in the halo profile were examined.

Grade migration can provide a pileup diagnostic. Smith et al. (2002) looked at the grade 0/grade 6 ratio as a pileup diagnostic for and observation of a bright source on the ACIS-I array. This diagnostic will be examined below.

A. Vikhlinin[7] suggested an approach estimating the QE suppression from pileup in the limit of mild pileup: since each piled up event corresponds to at least two photons the QE suppression can be estimated to be at least $2 \times g_{157}/g_{02346}$ where g_{157} is the sum of the *ASCA* "bad" (1,5,7) grades and g_{02346} is the sum of the *ASCA* "good" (0,2,3,4,6) grades; particle background, which has a different grade distribution, must also be accounted for. This suggests that the "bad/good" ratio, g_{157}/g_{02346}, could also be used as a pileup indicator.

I plot in Fig. A.1 the bad/good ratio as a function of energy for X-ray events and for particle background events. The values for X-ray events are based on ACIS-S3 ground (subassembly) testing[8]. The good/bad ratio for background particle events is based on blank sky background and "stowed" background level 1 datasets provided by M. Marke-

[7] Internal memo.

[8] http://cxc.harvard.edu/cal/Acis/Cal_prods/branch/pre_flight/pre_flight.html

vitch[9] The bad/good ratio for X-ray events is $\sim 1-2\%$ at low energies, and gradually reaches $\sim 9\%$ at high energies. In the background datasets, the ratio is $\sim 10\%$ at low energies, but rapidly climbs above ~ 5 keV. This suggests that for soft sources with emission mainly ≤ 5 keV, filtering the energy to $E \leq 5$ keV would reduce the effect of background in deriving the bad/good (g_{157}/g_{02346}) ratio.

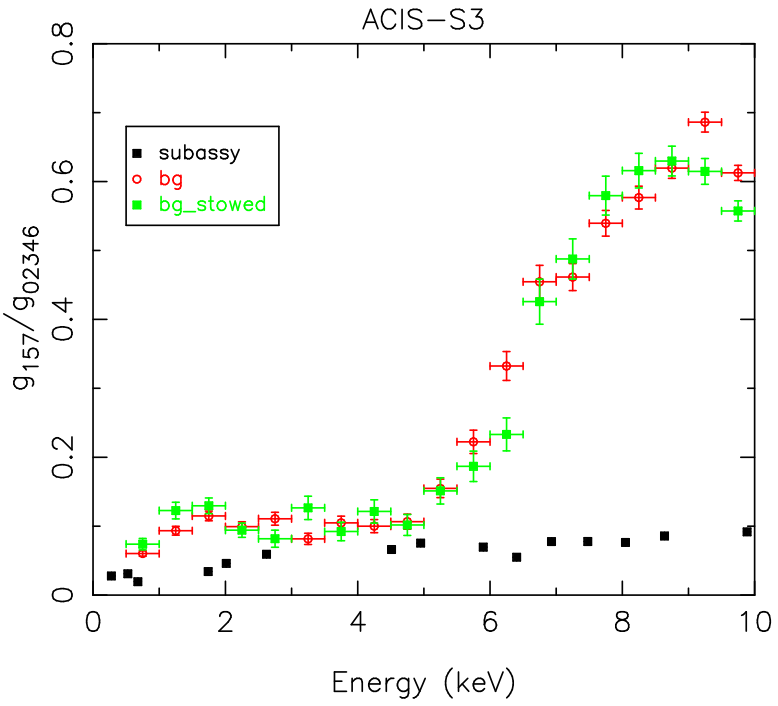

Figure A.1: Ratio of *ASCA* "bad" grades to *ASCA* "good" grades for ACIS-S3 subassembly data and ACIS-S3 on-orbit background data. The *subassy* data are from subassembly calibration test during ground testing. The *bg* and *bg_stowed* datasets are level 1 background datasets. *bg* is blank sky background, and *bg_stowed* is background taken when ACIS was out of the focal plane and not exposed to the sky. See text.

In the case of Her X-1 the spectrum is very soft, with most of the emission below ~ 1 keV. For moderate pileup in the near wings, most of the detected piled up events will have energies less than ~ 2 keV. Evaluating the grade ratio for energies between 0.5 and 2 keV emphasizes the grade migration of X-ray events, while reducing the contamination from the background events at higher energies.

In the left panel of Fig. A.2 the radial profiles of bad events and good events are plotted for the Her X-1 observation, and in the right panel the corresponding bad/good ratio is plotted. The profiles are based on the level 1 event list after filtering on energy ($0.5-2.0$ keV) to reduce the inclusion of particle events. In the left panel, the bad events

[9]private communication.

dominate inside $\sim 2-3''$; at larger radii the bad events fall more rapidly than the good events. Beyond $\sim 100''$ the profile for the bad events levels off. The trends can be seen more clearly in the ratio plot in the panel on the right. The rapid rise inside $\sim 15''$ indicates that pileup increases in importance and then dominates the distribution. Inward of $2''$ the grade migration is severe and in the core, all events are lost. From $\sim 15''$ to $\sim 100''$ the profile is dominated by valid X-ray events with a low bad/good ratio characteristic of the photons in the $0.5-2.0$ keV band. Beyond $\sim 100''$ particle background is becoming important, which produces the upward trend in the bad/good ratio.

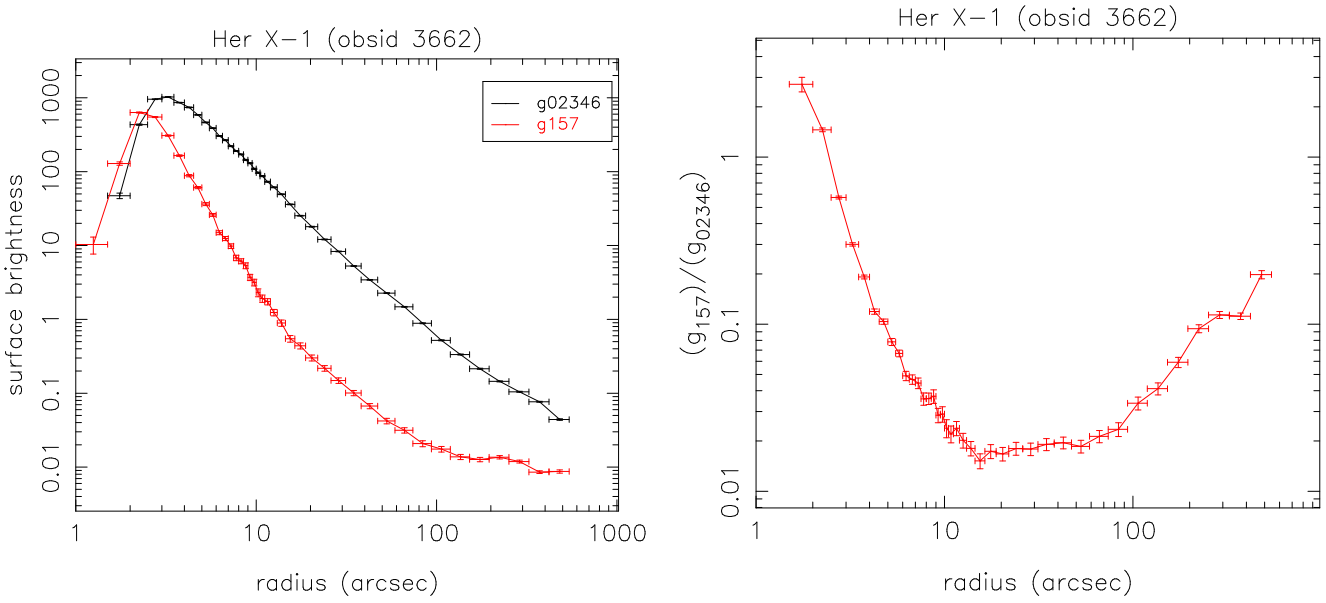

Figure A.2: s
ubassembly data and on-orbit background.] Left: Her X-1 data. Surface brightness profiles for *ASCA* good grades and *ASCA* bad grades. Status filtered and energy filtered $0.5-2.0$ keV. No exposure correction applied. Right: Her X-1 data: as in bottom left figure, but showing the ratio of *ASCA* bad grades to *ASCA* good grades.

I also examined other approaches to assessing pileup, and examined modified versions of diagnostics used in Smith et al. (2002).

Grade migration for a source imaged on the ACIS-I array was examined in Smith et al. (2002); the behavior of the ratio of *ASCA* grade 0 to the sum of *ASCA* good grades (0, 2, 3, 4, 6), and the corresponding ratio for grade 6 seemed to provide a good diagnostic. With grade migration single-pixel events (grade 0) migrates to other grades, and particularly grade 6. The decrease of the grade 0 fraction and the the increase in the grade 6 fraction toward the core of the image was taken as an indication of pileup; the grade fractions became asymptotically flat at large radii.

The Her X-1 ObsID 3662 images the source on the back-illuminated chip ACIS-S3, and the g_0/g_6 criterion is not as distinctive as for the FI chips; background makes a more significant contribution. I examined the grade fractions as a function of radius, and found

that the grade 6 fraction decreases radially outward, reaches a minimum, then increases. Similarly, the grade 0 fraction increases, reaches a maximum, then decreases. I examined grade ratios as a function of energy, and also examined grade ratios for background datasets. The particle background has a significantly larger fraction of grade 6 events, particularly above ~ 2 keV. As in the case of the "bad/good" ratio test discussed above, the peculiarity in the grade ratio profiles is a result of the increasing importance of background events with increasing radius. Again, filtering on energy ($0.5 - 2.0$ keV produces a cleaner evaluation of the diagnostic. The grade 6 and grade 0 profiles are plotted in the left panel of Fig. A.3. This diagnostic suggests that pileup is important inside $\sim 8''$.

Finally, a crude estimate can be made based on Poisson statistics (Smith et al., 2002). For the diffuse scattered emission, I estimate the source rate such that there is a 5% probability that two events will land in a 3×3 pixel island within a single frame (3.1 s for ObsID 3662). This is only approximate, since the diffuse emission is not uniform. In the right panel of Fig. A.3, the radial profile for the Her X-1 ObsID 3662 observation is plotted, and the Poisson-based pileup estimate is indicated as a horizontal line. Moving radially inward, the profile peaks, then plummets to zero as pileup becomes extreme and all events are morphed into bad events. Based on this diagnostic, I estimate that pileup is becoming significant $\sim 8''$ from the source.

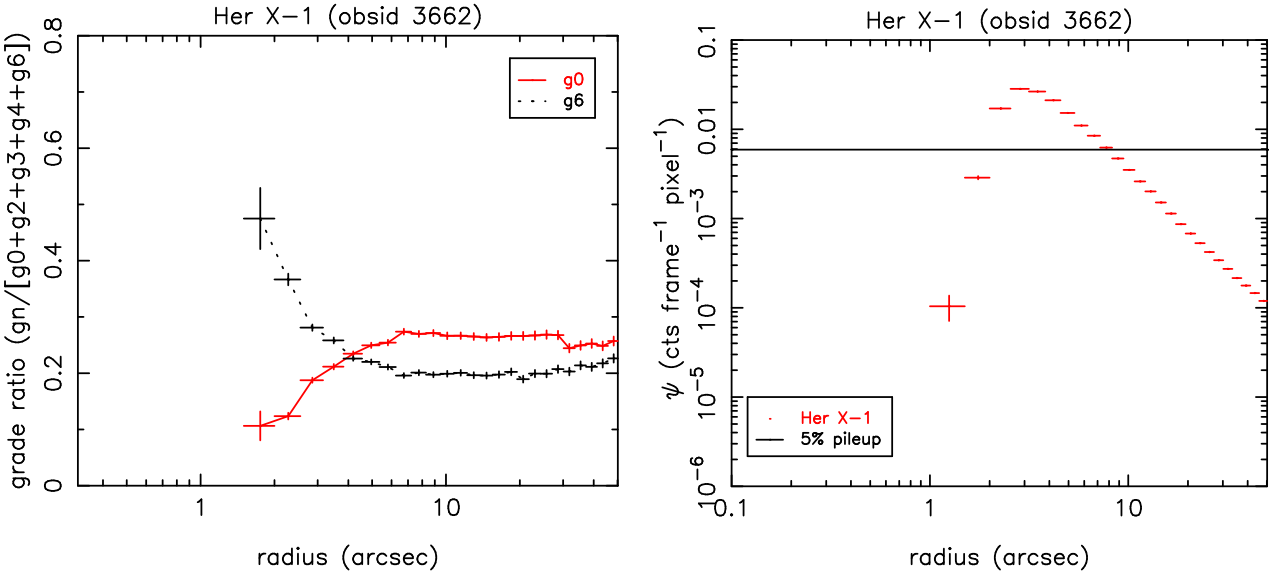

Figure A.3: Left: Profiles of the ratios of grades 0 and 6 to the sum of grades 0, 2, 3, 4, and 6 for ObsID 3662. Right: Her X-1 ObsID 3662 surface brightness profile; the horizontal line indicates an estimate of the rate at which pileup is $\sim 5\%$.

Comparing the various pileup estimates, the "bad/good" ratio diagnostic is the most sensitive. I conclude that pileup is likely a significant factor inside $\sim 8''$, and possibly as far out as $\sim 15''$. To be conservative, the profiles are fit only for $\theta \geq 15''$, but the extrapolated profile still fits reasonably well inward of $15''$.

B The ACIS Transfer Streak

At the Colorado HEAD meeting (Estes Park, 1997), M. Bautz suggested making use of the ACIS transfer smear during frame readout to allow photon counting for heavily piled up sources. The following describes how this can be used to estimate the source rate for a heavily piled up point source.

ACIS accumulates events for a frame exposure time (`EXPTIME`, 3.1 s for this observation), then rapidly reads out the frame with a parallel transfer rate of 40μs per row; the parallel transfer time for a full frame is 0.04104 s (the difference between the `TIMEDEL` and `EXPTIME` values). Because there is no shutter, the CCD still accumulates events during the frame transfers; each pixel thus samples the source plus background along the whole column, accumulating charge as the packet is clocked over the source distribution. Normally the transfer streak is not noticeable except in the case of bright point sources. In general, however, it affects every pixel in every column: ihe exposure for each pixel includes a scaled-down sum of the source plus background for its column.

Any given pixel picks up part of its transfer-streak charge while being clocked in at the beginning of the frame (the portion closer to the frame store), and part while being clocked out at the end of the frame (the portion further from the frame store). The transfer streak thus extends both directions from sources.

Because the frame accumulation time (≤ 3.2 s) is much shorter than the dither timescale ($\sim 10^3$s), the projected sky position shifts by only a small fraction of a pixel during a single frame. The transfer streak can be considered as effectively instantaneous as far as dither is concerned, even though part of the transfer streak exposure is accumulated at the beginning of a frame and part at the end of a frame.

B.1 Estimating the Transfer Streak Spectrum

To utilize the transfer streak:

- Extract a narrow region in the direction of the transfer but excluding regions near the core of the image where events are piled up (see Fig. B.1).
- Evaluate the source count rate in the transfer streak (number of events in the pixel/packet dwell time).
- Subtract a corresponding background count rate, scaled for the background exposure time and extraction area.
- Correct for the effective "duty cycle" for the frame transfer. The streak extraction area is N pixels long, and the pixel dwell time for parallel transfer is 40μ s per pixel. The duty cycle is thus $N \times 40\mu\,\mathrm{s}/t_{frame}$ where t_{frame} is the frame collection time (3.1 s for the Her X-1 observation. Note that the background subtraction occurs *before* correcting for the frame transfer duty cycle; almost all background events will have occurred during the frame collection rather than during the parallel transfer.
- In principle, a correction for PSF sampling in the transverse direction and contribution of the wings in the streak direction should also be applied. This has not been done at this time. The expected correction is smaller than other systematic uncertainties. Such corrections could be done as follows:

– evaluate the line PSF based on the core of the PSF and the width of the transfer streak clipping region. The ACIS-S and ACIS-I arrays have different clocking directions, so two versions of the correction factor will have to be evaluated.
– The contribution of the wings to the transfer streak can be evaluated by using a fit to the wings from regions excluding the transfer streak.

Currently, these corrections are not applied.

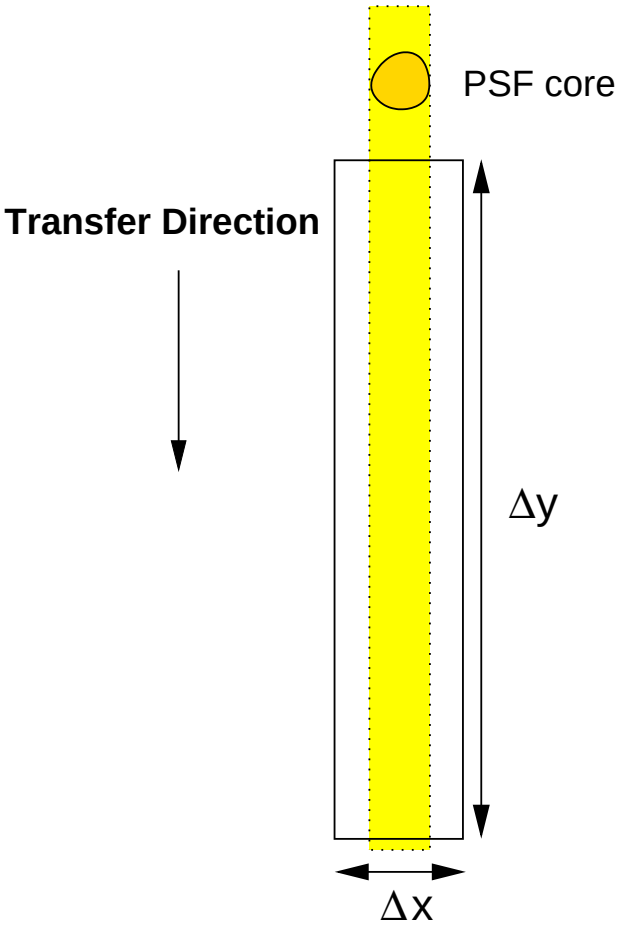

Figure B.1: Schematic of the transfer streak calculation. Δx should be large enough to include the core and near wings, but small enough to minimize the enclosed background. Δy should extend over a region far enough away from the source that the included wing profile is small compared to the transfer streak contribution. A corresponding box on the other side of the direct image can be added to improve the statistics.

B.2 Evaluating the Her X-1 Transfer Streak Spectrum

In the case of the Her X-1 observation, 15994 frames were accumulated (determined from the number of unique `EXPNO` values). The streak spectrum is extracted from a 10″

wide region, 609 pixels in length, centered on the bright core of the transfer streak. The accumulated exposure time in the streak during frame transfer is $609 \times 15994 \times 4 \times 10^{-5} = 389.614\,\mathrm{s}$. Rates estimated from the spectrum need to be scaled by 127.298, the ratio of observation exposure time (49579.136 s) to the effective streak exposure time for the extracted streak spectrum (389.614 s); the inverse of this ratio is the effective duty cycle for frame transfer.

The rate for each energy range is determined by integrating over `PI` column in the spectrum file, treating the distribution as a piecewise constant function of `PI`. A gain correction is applied. In simultaneous fits to *Chandra* transfer streak data and *RXTE* data, Heinke et al. (2003) found they needed a shift in the slope of the gain function of $7\% \pm 1\%$. My fits to the Her X-1 (ObsID 3662) transfer streak data indicate a gain shift of $\sim 2.5\%$. Simultaneous fits to transfer streak data for an observation of 3C273 on ACIS-S3 without the grating (ObsID 1712) and MEG data for 3C273 (ObsID 2463) suggest a gain slope offset of $\sim 3\%$. These estimates for the gain slope shift are dominated by the shift in position of the Ir Mv edge at ~ 2.1 keV; in the Terzan 5 data analyzed by Heinke et al. (2003) the statistics for this edge , and there is significant flux in the region of overlap with the RXTE spectrum ($E \geq 3$ keV). The reason for the larger slope shift obtained by Heinke et al. (2003) is not currently understood; a possibility is a calibration offset between the two observatories. In any event, the properties of the ACIS transfer streak spectrum needs to be studied more systematically. Given the uncertainties, for the present analysis a linear slope shift of 2.5% with no offset is used:

$$E_{corr} = (1 + \alpha)E \tag{5}$$

where $\alpha = 0.025$.

The background-subtracted rate in an energy bin ΔE_k is estimated as:

$$\mathcal{S}_{streak}(\Delta E_k) \simeq \frac{f_{xfr,streak}}{ARF_{src,corr}(\Delta E_k)} \left[\frac{C_{streak}(\Delta E_k)}{t_{exp,src}} - \frac{C_{bgd}(\Delta E_k)}{t_{exp,bgd}} \right] \qquad (\mathrm{cts\ cm^{-2}\ \ s^{-1}}) \tag{6}$$

where $C_{streak}(\Delta E_k)$ the number of counts in the streak extraction region and $C_{bgd}(\Delta E_k)$ is the number of counts for the same region in the background dataset; $t_{exp,src} = 50\,\mathrm{ks}$ is the exposure time for the Her X-1 wings observation, and $t_{exp,bgd} = 350\,\mathrm{ks}$ is the exposure time for the blank sky background data. The $ARF_{src,corr}(\Delta E_k)$ term is the value of the ARF (with a spatially independent correction for the ACIS contamination) summed over `PI` and averaged over a $10''$ radius circle centered on the Her X-1 specular image. The correction used A. Vikhlinin's `corrarf` with the qe_cor.H20.C10.O2.N1 contamination model, which is based on G. Chartas' `ACISABS` corrector. The factor

$$f_{xfr,streak} = \frac{3.1\,\mathrm{s}}{609\ \mathrm{rows} \times 40\,\mu\mathrm{s\,/row}} = 127.298 \tag{7}$$

is the inverse of the effective duty cycle for frame transfer through the streak extraction region (609 rows in the parallel transfer direction).

B.3 Pileup in the Her X-1 ACIS Transfer Streak

Alexey Vikhlinin (internal memo, 2004) suggested that QE depression from pileup (in the low pileup limit) can be estimated by comparing the *ASCA* "good" grades (grades 0, 2, 3, 4, and 6) to the *ASCA* "bad" grades (grades 1, 5, and 7). Since each bad event, if generated by pileup, corresponds to at least two photons, the ratio $2g_{157}/g_{02346}$ is an estimate for the minimum QE depression caused by pileup. (Background events have a different grade distribution than X-ray events, so the effect of background on the estimate needs to be taken into account; see Appendix A.)

For the level 1 event list, a narrow region centered on the transfer streak is examined. The region is 4 pixels by 984 pixels, and a circular region 40 pixels in radius centered on the specular image of Her X-1 is also excluded. The grade ratio for these events is $g_{157}/g_{02346} \simeq 0.039$, implying an effective QE loss of $\sim 8\%$. The rate per frame in the transfer streak is estimated by examining the statistics of counts within the region; The mean rate is 9.40 ± 3.85 cts/frame. A simple Poisson estimate based on at least one additional photon hitting the location of a detected event or one pixel to either side (as the event is clocked through) is $\sim 4.1\%$. The pileup fraction for the transfer streak is thus estimated as $\sim 4\%$. The normalization factors for the Her X-1 profiles have been scaled by 1.08 to account for this effect.

C Exposure Correction and Effective Area

In principle, the effective area which should be used varies depending on the origin of the event:

- For directly (*i.e.*, specularly) imaged photons from astrophysical sources, A_{eff} appropriate to the detected position should be used.
- For photons scattered by the mirrors (mirror scattering halo), the A_{eff} appropriate to the location of the specular image of the source should be used; the vignetting function implicitly includes the mirror scattering contribution.
- For particle background events A_{eff} should not be used since these are not imaged X-rays. If these events are subject to vignetted at all, the vignetting will be in completely different way than for imaged X-rays.
- For ACIS transfer streak events, the A_{eff} appropriate to the location of the specular image of the source should be used; the X-ray actually hit the the detector at the direct image, and its detected position is an artifact. In general, it is not possible identify likely transfer streak events unless there is a single bright source in the column.

In practice, it is not possible to distinguish reliably events resulting from mirror-scattered photons from particle background events or from directly imaged sky photons from diffuse emission. Thus, it is not possible to apply a different A_{eff} depending on what produced the event, so compromises are needed. In any case, treatment of vignetting for background events should be consistent with the treatment of the source events.

In this work, the correction for effective area and detector QE is done in two distinct ways:

- For study of the mirror PSF properties, one wants to get to the intrinsic mirror performance. The deep wings observation provides good statistics so that the mirror scattering wings generally dominate over the background. In this case, the effective area at the specularly imaged position of the source is used, rather than that associated with the detected position. The image is flattened using a projected instrument QE map (incorporating the aspect solution but *not* the HRMA vignetting). The effective area (including vignetting) is instead evaluated at the position of the specular image of Her X-1. For consistency, the flattening of the blank sky background data is done the same way. These results are reported in §4.
- For studies of source extent or diffuse emission, the diffuse emission may be significant compared to the mirror scattering contribution. As noted above, it is not possible to categorize events uniquely into events resulting from mirror scattering, events resulting from diffuse astrophysical emission, and detector background. Typically, one might apply the mirror vignetting correction in the computation of the exposure map, even though it is not strictly applicable to those events resulting from mirror scattering or detector background. Again, for consistency, the flattening of the blank sky background would be done in the same way, even though the particle background component would not be vignetted in the same way as X-ray events. For comparison, results applying this approach are reported in Appendix D.

D Fits Including Mirror Vignetting

Although the mirror vignetting function should not be applied to photons which are scattered by the mirror, in some analyses it is necessary to do this. For studies of source extent or diffuse emission, the diffuse emission may not be negligible compared to the mirror scattering contribution. It is generally not possible identify a given event unambiguously as a photon from a specular source scattered by the mirrors, a photon from diffuse astrophysical emission (*e.g.*, source extent, or a diffuse cosmic dust scattering halo), or a background particle event. If the analysis requires applying the vignetting function to the data, then vignetting would need to be applied to the mirror scattering (and background) data.

In this appendix, an analysis is presented which includes the mirror vignetting in addition to the detector QE when generating the exposure correction. For consistency, the exposure correction for the background data set now also includes the mirror vignetting. The profiles are calculated as

$$\langle \psi_{src} \rangle_{\Delta\theta_i} = \frac{\left\langle C'_{src,corr} \right\rangle_{\Delta\theta_i}}{t_{src,exp}} \tag{8}$$

where $C'_{src,corr} = C_{src,counts}/A_{eff} q \mathcal{Q}$ is the vignetting and QE-corrected counts image. The A_{eff} is now the effective area at the detected position, see §C; t_{exp} is the exposure time, and q is a correction factor for the low-energy QE degradation at the time of the observation (very close to 1 for $E \gtrsim 1$). The $\langle\rangle_{\Delta\theta_i}$ again indicates an average over annulus i of width $\Delta\theta_i$. The surface brightness for background is constructed in the same way using the sky background dataset:

$$\langle \psi_{bgd} \rangle_{\Delta\theta_i} = \frac{\left\langle C'_{bgd,corr} \right\rangle_{\Delta\theta_i}}{t_{bgd,exp}} \tag{9}$$

where $C'_{bgd,corr} = C_{bgd,counts}/A_{eff} \mathcal{Q}$; The low-energy QE correction term, q, is not applied. The PSF's are normalized as described in §subsec:normalizing.the.profiles, and the normalized profiles have units arcsec^{-2}.

The wing profile is fit by a powerlaw plus exponential cutoff plus spatially constant background:

$$\psi(\theta) = a \left[\frac{\theta}{\theta_0} \right]^{-\alpha} \exp\left(c\theta\right) + b \tag{10}$$

where b is the background component, a is the wing amplitude scale factor, α is the powerlaw slope, and $1/c$ is the exponential cutoff scale length. The fit is scaled to a reference radius, $\theta_0 \equiv 10''$. The background datasets are fit with the a parameter frozen at 0. The resulting fit parameters are shown in Table D.1, and the profiles plotted in Figs. D.1–D.4.

Table D.1: Fit Parameters. (Note: errors are purely statistical.)

Energy (keV)	γ	a (ct arcsec^{-2})	c (arcsec^{-1})	b (ct arcsec^{-2})	χ^2(dof)
1.0-2.0	1.967 ± 0.003	$(0.744 \pm 0.004) \times 10^{-05}$	$(-0.564 \pm 0.049) \times 10^{-03}$	$(0.391 \pm 0.003) \times 10^{-08}$	221(70)
2.0-3.0	1.841 ± 0.004	$(1.013 \pm 0.007) \times 10^{-05}$	$(-1.075 \pm 0.060) \times 10^{-03}$	$(0.547 \pm 0.005) \times 10^{-08}$	87(70)
3.0-4.0	1.764 ± 0.008	$(1.884 \pm 0.016) \times 10^{-05}$	$(-1.836 \pm 0.052) \times 10^{-03}$	$(0.683 \pm 0.007) \times 10^{-08}$	132(70)
4.0-5.0	1.757 ± 0.008	$(2.591 \pm 0.022) \times 10^{-05}$	$(-1.823 \pm 0.051) \times 10^{-03}$	$(0.872 \pm 0.009) \times 10^{-08}$	81(70)
5.0-6.0	1.924 ± 0.011	$(3.533 \pm 0.038) \times 10^{-05}$	$(-1.473 \pm 0.074) \times 10^{-03}$	$(1.487 \pm 0.015) \times 10^{-08}$	153(70)
6.0-7.0	2.002 ± 0.016	$(4.166 \pm 0.061) \times 10^{-05}$	$(-1.057 \pm 0.117) \times 10^{-03}$	$(3.530 \pm 0.033) \times 10^{-08}$	164(70)
7.0-8.0	2.264 ± 0.032	$(5.303 \pm 0.139) \times 10^{-05}$	$(2.031 \pm 0.255) \times 10^{-03}$	$(18.425 \pm 0.131) \times 10^{-08}$	269(70)

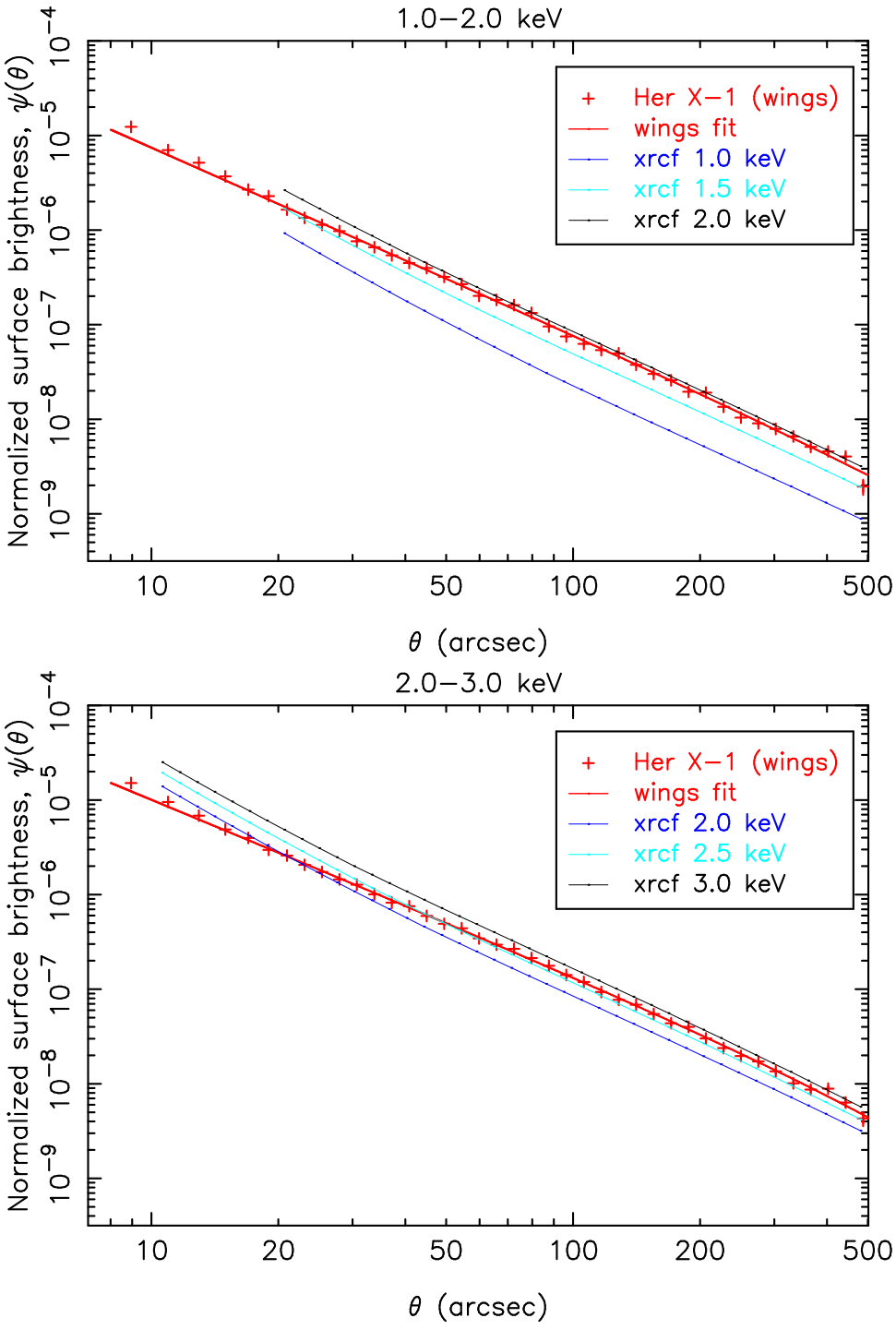

Figure D.1: Powerlaw plus exponential cutoff fits to the obsid 3662 (Her X-1 wings) data; the fits were for $\theta \geq 15''$. Mirror vignetting was included in exposure correcting the data (see text). The model based on ground calibration data is also indicated (labeled "xrcf"). Top: 1.0-2.0 keV. Bottom: 2.0-3.0 keV.

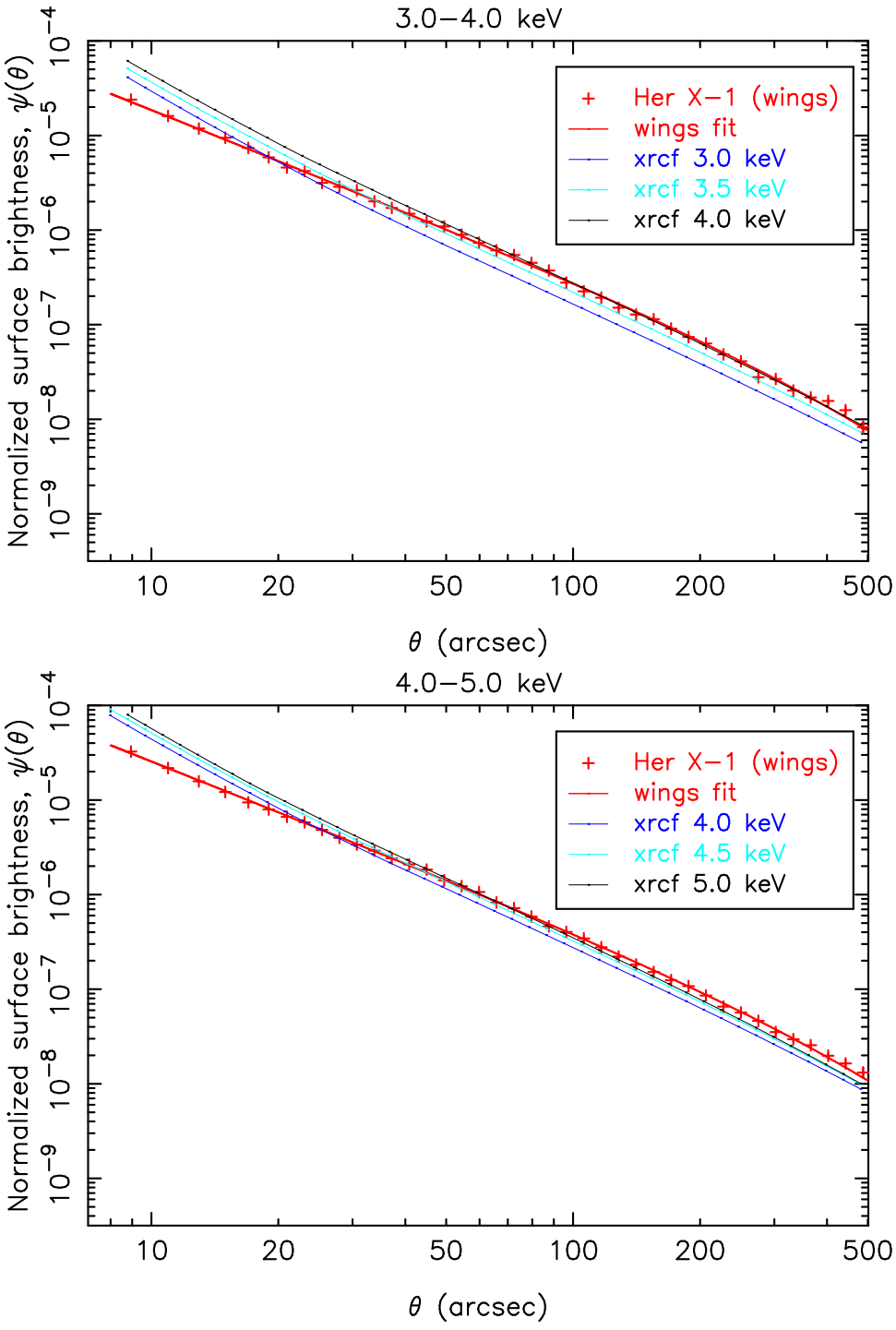

Figure D.2: Powerlaw plus exponential cutoff fits to the obsid 3662 (Her X-1 wings) data; the fits were for $\theta \geq 15''$. Mirror vignetting was included in exposure correcting the data (see text). The model based on ground calibration data is also indicated (labeled "xrcf"). Top: 3.0-4.0 keV. Bottom: 4.0-5.0 keV.

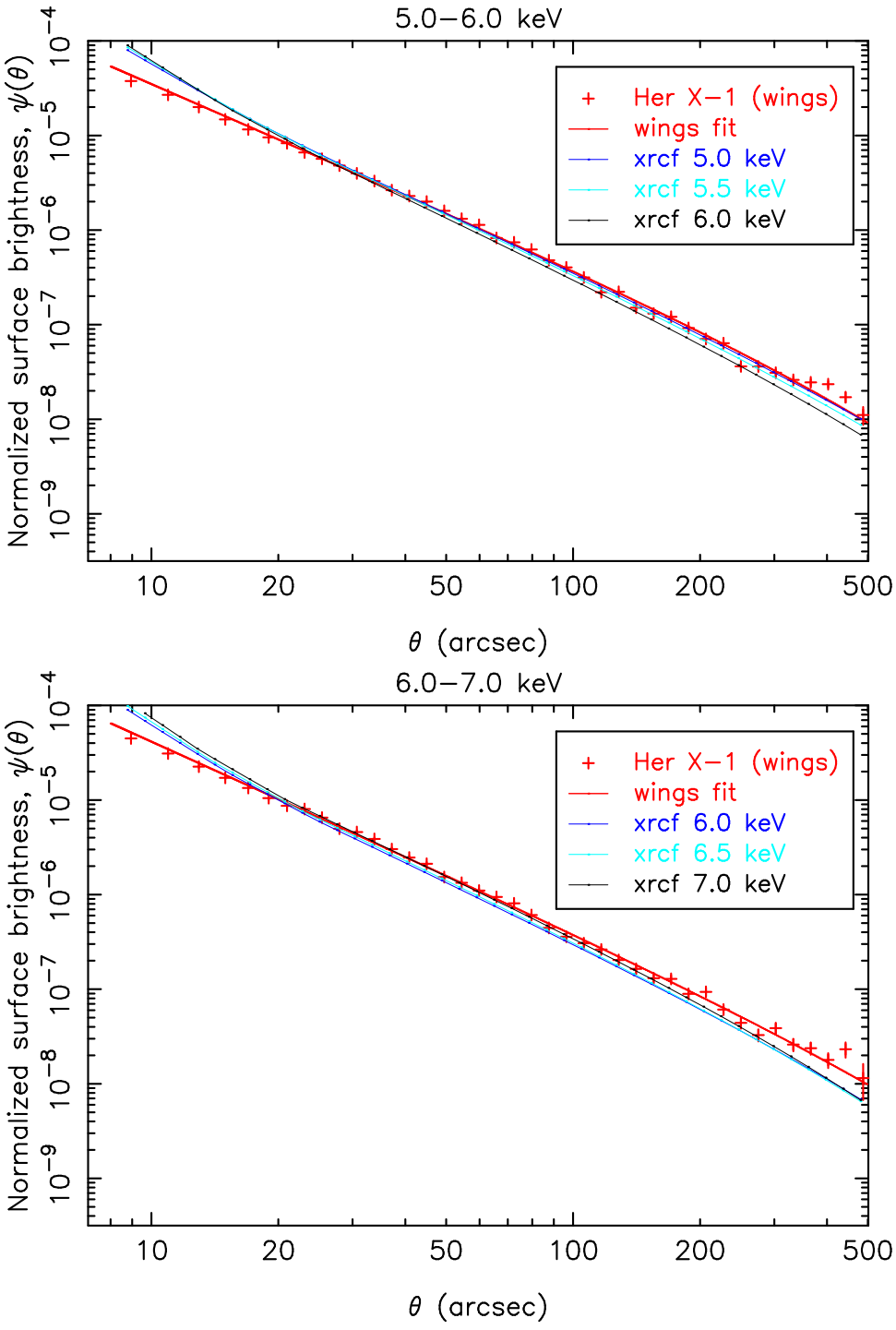

Figure D.3: Powerlaw plus exponential cutoff fits to the obsid 3662 (Her X-1 wings) data; the fits were for $\theta \geq 15''$. Mirror vignetting was included in exposure correcting the data (see text). The model based on ground calibration data is also indicated (labeled "xrcf"). Top: 5.0-6.0 keV. Bottom: 6.0-7.0 keV.

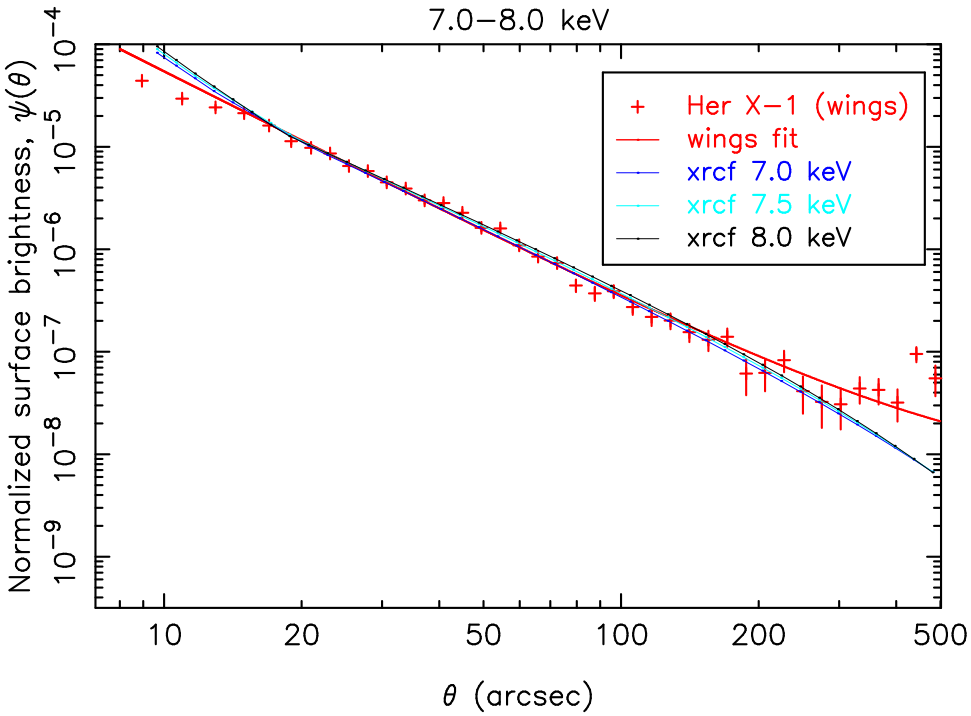

Figure D.4: Powerlaw plus exponential cutoff fits to the obsid 3662 (Her X-1 wings) data; the fits were for $\theta \geq 15''$. Mirror vignetting was included in exposure correcting the data (see text). The model based on ground calibration data is also indicated (labeled "xrcf").

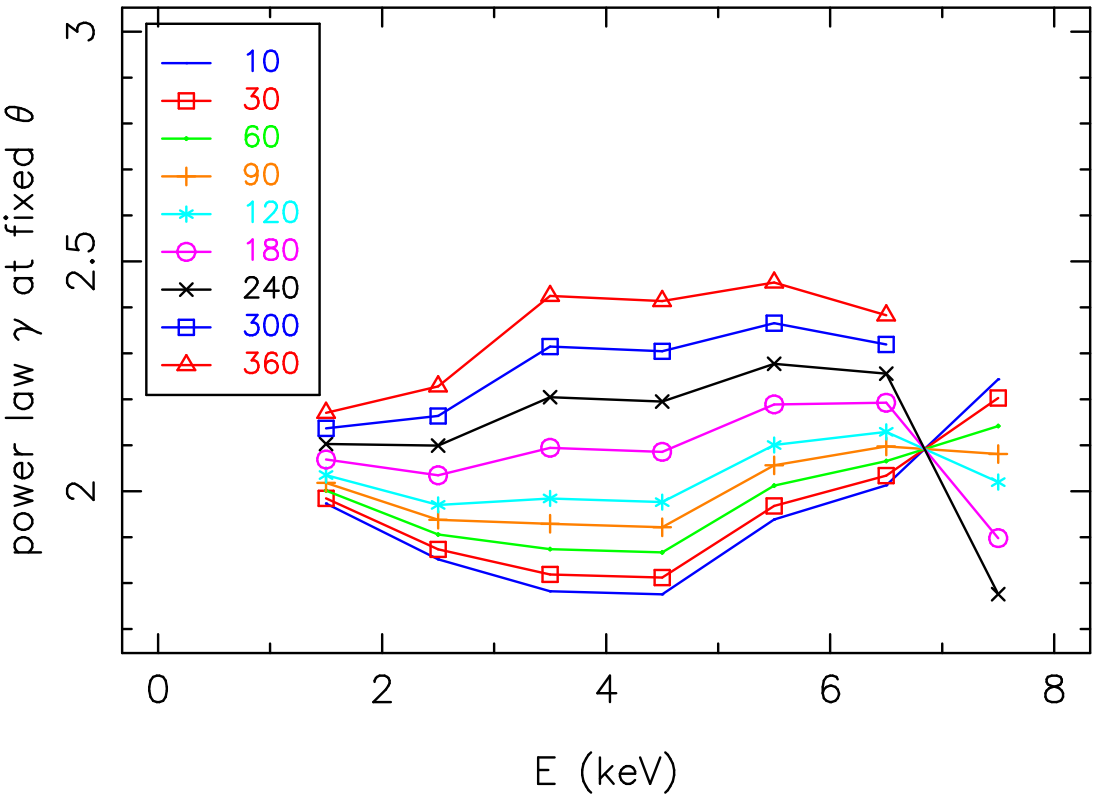

Figure D.5: Variation in local powerlaw slope. The curves are labeled by the value of θ in arcsec. The highest energy band (7–8 keV) is poorly constrained; the overall flatter profile and the extreme flattening seen at large radii likely reflect problems with background subtraction.

E Diffuse PSF Wings: spectral variations

The mirror scattering is in part diffractive, and the scattering angle depends on the incident X-ray energy. In Fig. E.1, the spectrum extracted from the bright core of the transfer streak (extraction width 10″) is plotted for reference. In Figs. E.2– E.4 the spectra for the diffuse mirror scattering emission are shown for annular extraction regions between 10″ and 400″. The annuli exclude a narrow 16 pixel wide strip centered on the bright core of the ACIS transfer streak, and also any regions falling off the ACIS-S3 detector (allowing for dither).

In the following figures, the spectral variation with E is particularly evident in the structure for $E \lesssim 2$ keV.

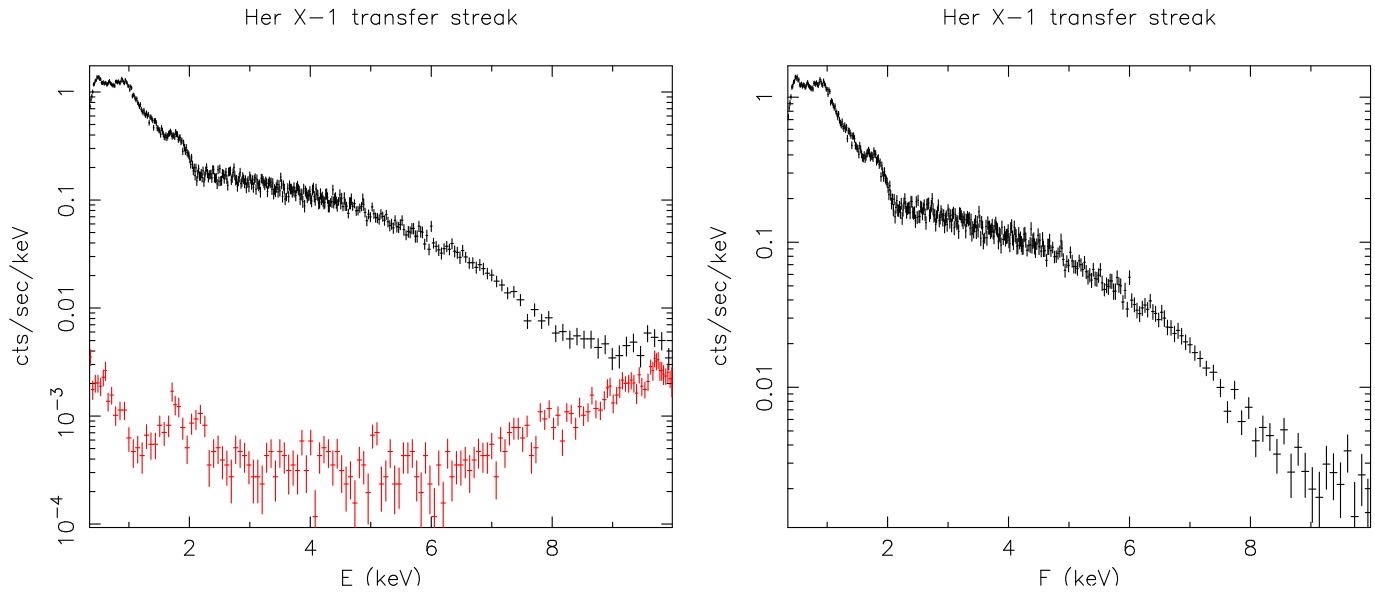

Figure E.1: Spectrum for the bright core of the Her X-1 transfer streak. Left: top curve: streak spectrum; bottom curve: spectrum extracted from the corresponding region of the blanks sky data. Right: background-subtracted transfer streak spectrum. .

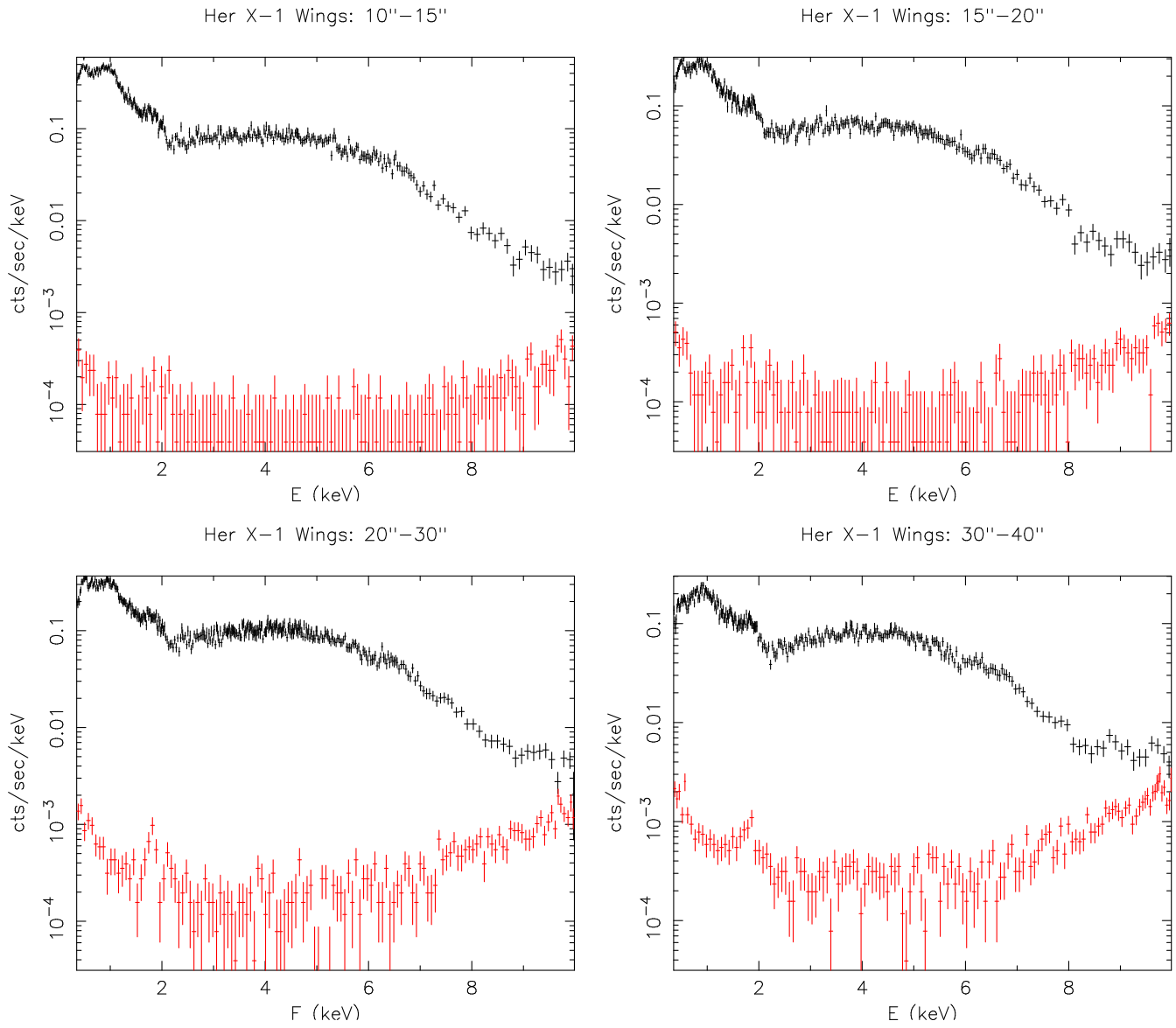

Figure E.2: Spectrum of the Her X-1 diffuse mirror scattering wings (excluding the core ACIS transfer streak). Top Left: $10'' - 15''$; source and blank sky. Top Right: $15'' - 20''$; source and blank sky. Bottom Left: $20'' - 30''$; source and blank sky. Bottom Right: $30'' - 40''$; source and blank sky.

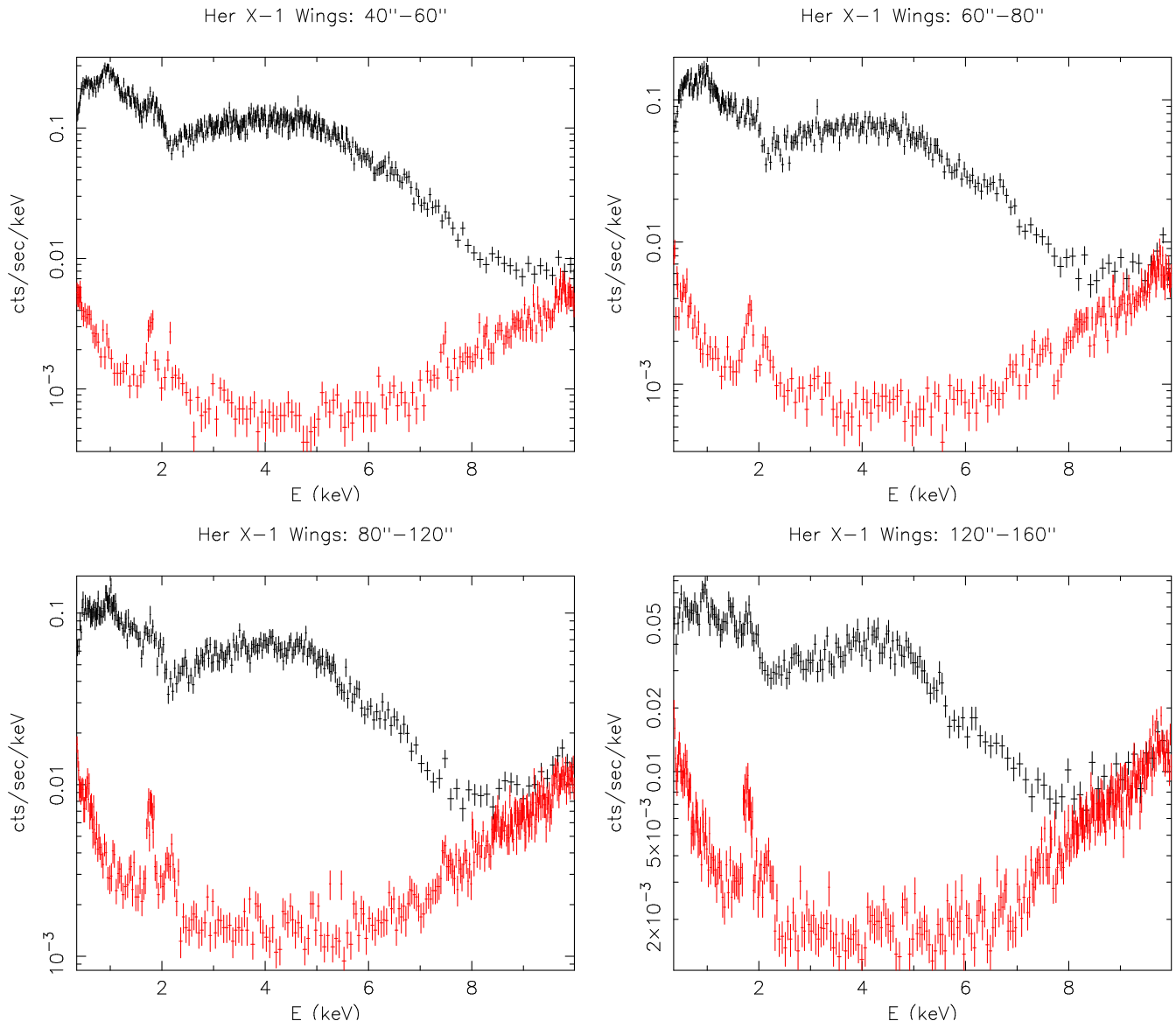

Figure E.3: Spectrum of the Her X-1 diffuse mirror scattering wings (excluding the core ACIS transfer streak). Top Left: $40'' - 60''$; source and blank sky. Top Right: $60'' - 80''$; source and blank sky. Bottom Left: $80'' - 120''$; source and blank sky. Bottom Right: $120'' - 160''$; source and blank sky.

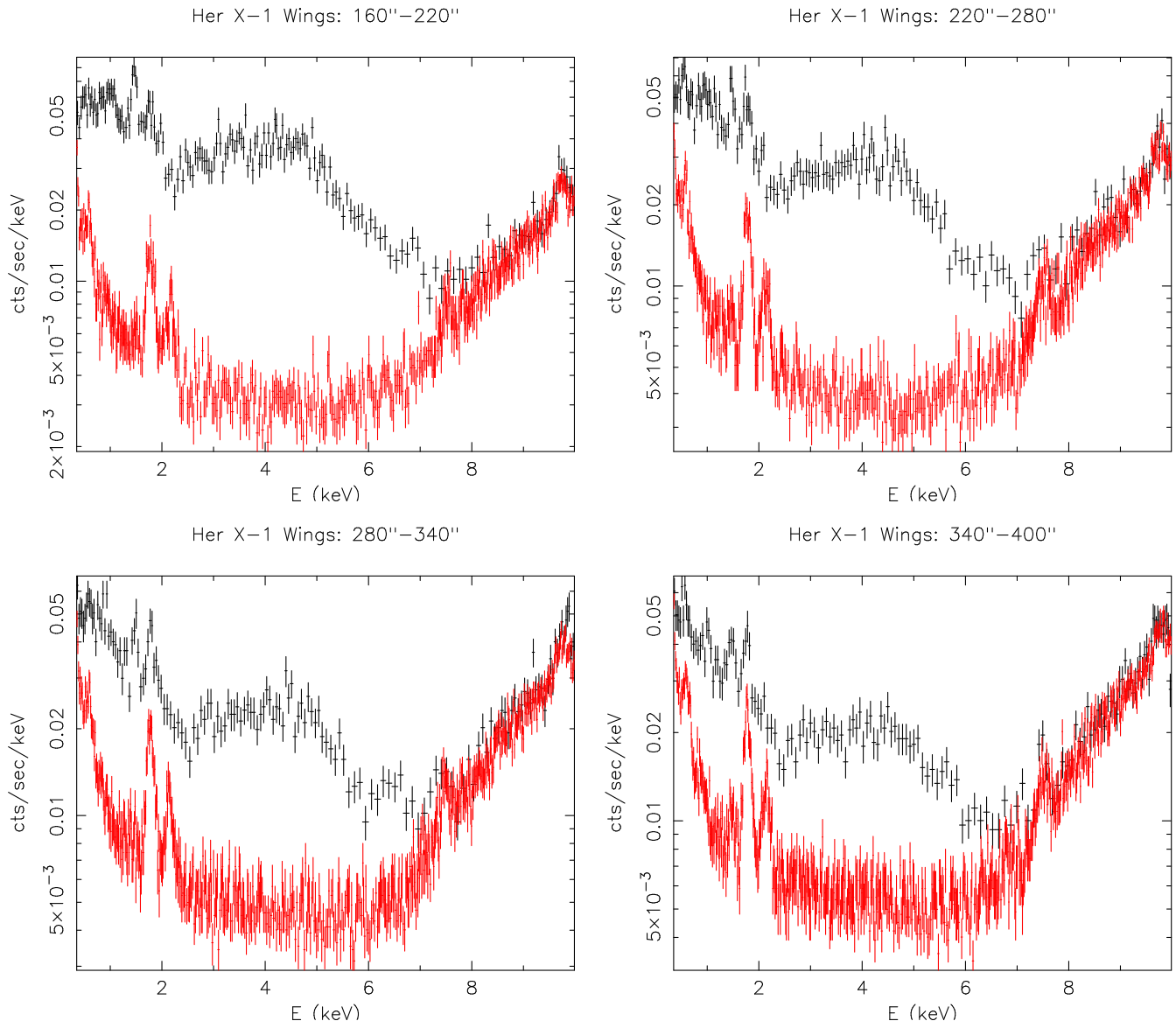

Figure E.4: Spectrum of the Her X-1 diffuse mirror scattering wings (excluding the core ACIS transfer streak). Top Left: $160'' - 220''$; source and blank sky. Top Right: $220'' - 280''$; source and blank sky. Bottom Left: $280'' - 340''$; source and blank sky. Bottom Right: $340'' - 400''$; source and blank sky.

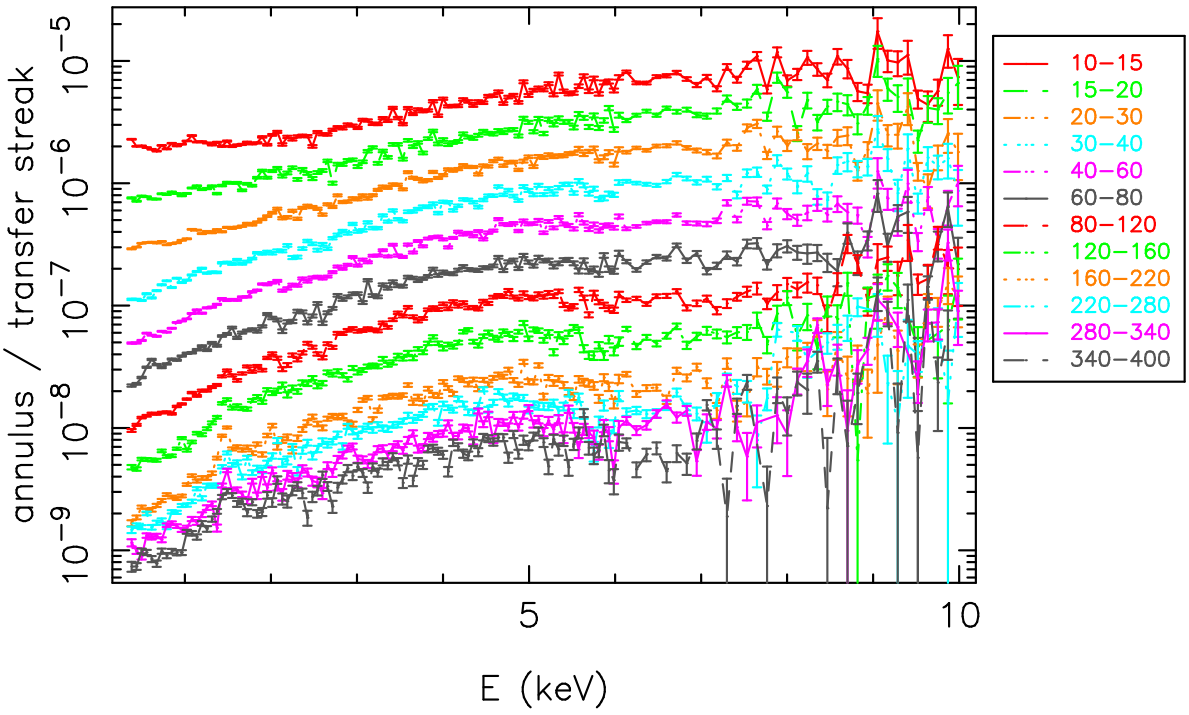

Figure E.5: Comparison of spectra for diffuse mirror scattering wing emission. The spectra extracted for annuli are normalized by a spectrum extracted from the transfer streak. The legend indicates the annular angles in arcsec. See the text for discussion. .

F Anomalous 1.5 keV line feature

For an initial investigation of the wings profile as a function of energy, a simple powerlaw fit was performed for the very narrow band X-ray image data (Fig. F.1).

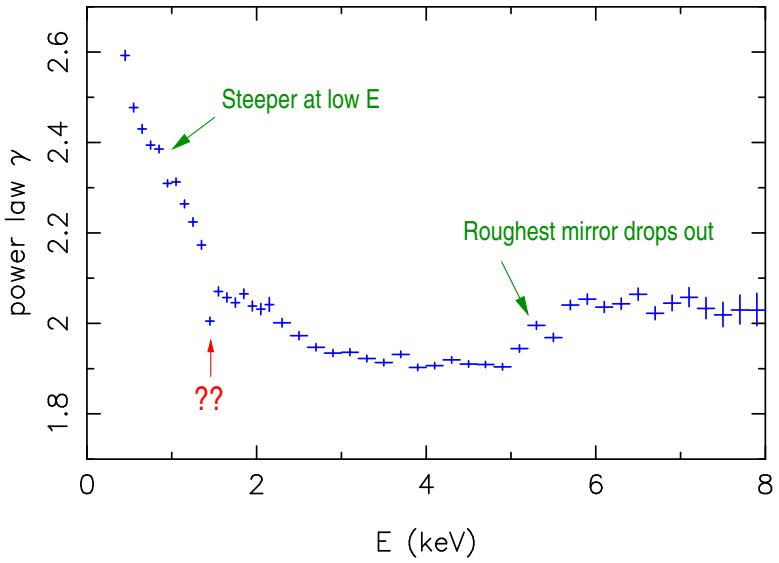

Figure F.1: Powerlaw index for fits to the narrow band obsid 3662 data.

The glitch at 1.5 keV deserves comment. There is no reason why the profile slope should be discontinuous at that energy. A possible explanation was revealed by examination of spectra of diffuse emission extracted from annular regions centered on the source. For radii beyond $\sim 2'$, the spectra show a pronounced line feature just below 1.5 keV (see Fig. F.2, left panel). This is not a feature in the Her X-1 spectrum — it does not appear in the transfer streak spectrum (see Fig. F.2, right panel). We believe this to be an artifact, since it is not evident in the sky background data, nor in the Her X-1 transfer streak data. Based on energy, it is tentatively identified as an Al Kα fluorescence feature, but there is no obvious source for the emission. The aluminum support struts in the central aperture plate are illuminated by Her X-1 and are in the view of the focal plane but the very small solid angle subtended by the detectors would seem to make this unlikely. Similarly, there is some aluminum in the optical blocking filter which is closer to the detector, but the aluminum is very thin (only ~ 1300 Å) so again it seems unlikely given the small optical depth and low fluorescent yield of aluminum. For now, we exclude the 1.4-1.6 keV band from the analysis of the obsid 3662 data and interpolate from the neighboring bands.

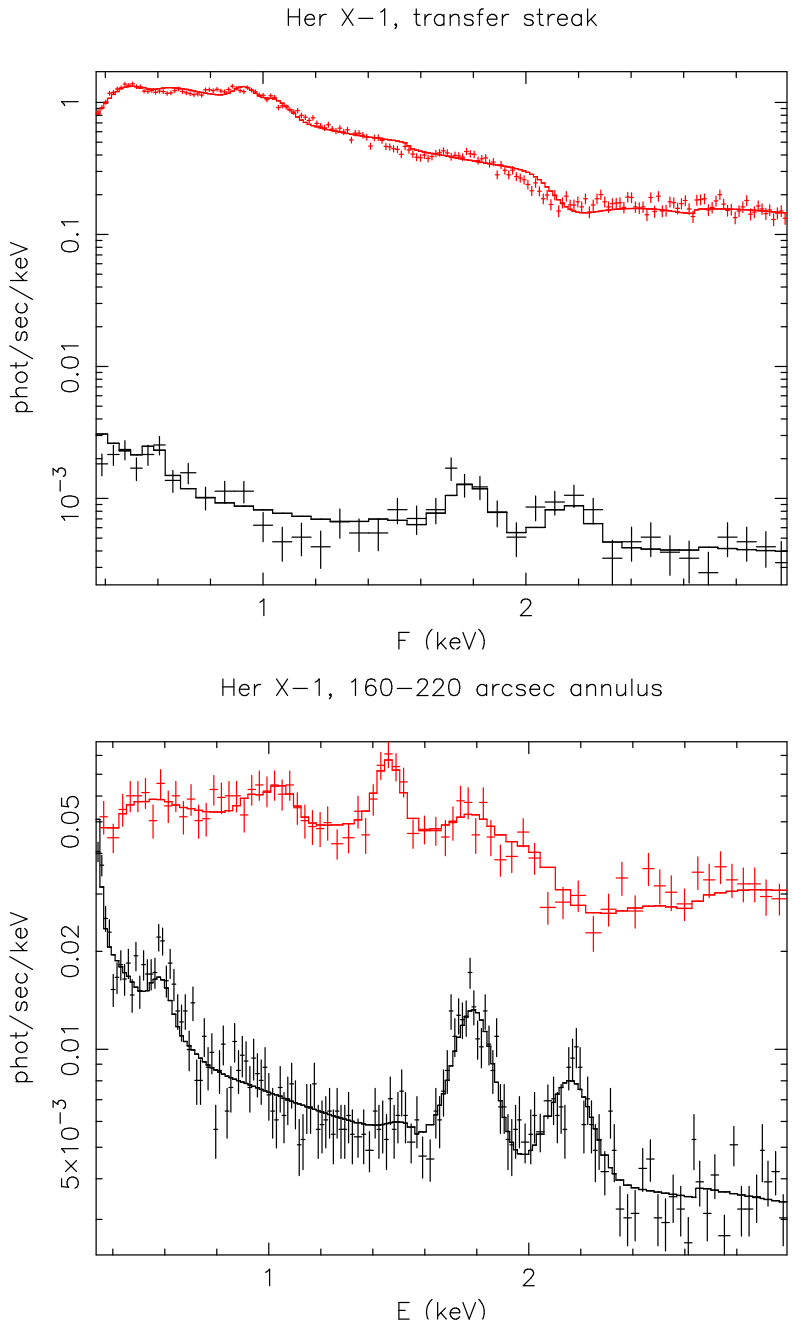

Figure F.2: Top: Spectrum for the transfer streak of Her X-1 (obsid 3662). Frame transfer is effectively a different ACIS mode, and it has not been calibrated. There is a shift in the slope of the gain of at least a few percent; this can be seen clearly at the Ir M edge just above 2 keV. (The rate has not been corrected for the effective transfer streak duty cycle.) Bottom: Spectrum for Her X-1 (obsid 3662) for an annular region 160–220″ from the source. In both panels, the upper curve is the Her X-1 obsid 3662 data. The lower curve shows the spectra for the corresponding blank sky data.